

Master Thesis Project
Report

pH sensing and Antibody detection with Surface Functionalized ISFETs

Submitted by

Dimitris Bardas
EE Master student
University of Twente

Under the guidance of

Loes Segerink
Full Professor
University of Twente

Sergii Pud
Assistant Professor
University of Twente

Rajendra P. Shukla
Postdoctoral Researcher
NC State University



ELECTRO  **Med**

Abstract

This Master Thesis project explores the multifaceted potential of Ion-Sensitive Field-Effect Transistors (ISFETs) in the area of peptide synthesis monitoring and biomolecule detection. By investigating the FETs suitability for the *in situ* pH tracking during peptide synthesis, this project aims to enhance the precision of biochemical processes. Furthermore, the study explores the detection of target biomolecules, specifically Antibodies, with the prospective goal of evaluating their affinity to peptide sequences. These advancements can contribute greatly to the integration of nano-FET technology into a cutting-edge platform that will assist the selection of neo-antigens for cancer vaccines within the framework of the "ElectroMed" project.

Contents

1	Introduction	2
1.1	Ion-Sensitive Field-Effect Transistors (ISFETs)	2
1.2	State-of-the-Art	4
1.3	Goals of the work	5
1.4	Report Overview	6
2	Theory	7
2.1	Field-Effect Transistors (FETs)	7
2.2	Accumulation mode SOI FETs	8
2.2.1	SOI FETs	8
2.2.2	Accumulation-mode FETs	8
2.2.3	Accumulation-mode ISFETs	12
2.3	pH theory	12
2.3.1	pH value	12
2.3.2	pH response of ISFETs	13
2.4	The solid-liquid interface - The Gouy-Chapman-Stern (GCS) model	16
2.5	Drift	19
2.6	Biomolecules	21
2.6.1	Amino Acids	22
2.6.2	Peptides	22
2.6.3	Peptide Synthesis	23
2.6.4	Antibodies	24
2.7	Surface functionalization	25
2.7.1	APTES	25
2.7.2	Boc Protecting Groups	27
3	Methods	30
3.1	pH Buffers	30
3.2	Chip encapsulation	30
3.3	pH Measurement Setup	31

3.4	Surface functionalization	33
3.4.1	APTES	33
3.4.2	Surface functionalization for pH-sensing	33
3.4.2.1	Boc / DeBoc	33
3.4.3	Surface functionalization for Antibody detection	34
3.4.3.1	Ester	34
3.4.3.2	"DYKGGGSH" peptide	35
3.4.4	Antibody detection	36
3.4.5	Negative control	36
4	Results	38
4.1	Experiments Overview	38
4.2	pH characterization	38
4.3	Surface functionalization	41
4.3.1	APTES	41
4.3.2	Surface functionalization for pH-sensing	43
4.3.2.1	Boc / DeBoc	43
4.3.3	Surface functionalization for Antibody detection	45
4.3.3.1	SMP - "DYKGGGSH" peptide	45
4.4	Antibody detection	46
4.5	Negative control	49
5	Conclusion	52
6	Outlook	53
	Acknowledgements	55
	References	56

Dedicated to my mother

Chapter 1

Introduction

1.1 Ion-Sensitive Field-Effect Transistors (IS-FETs)

Modern electronic devices and systems have been introduced and revolutionized human life by exploiting the merits of semiconductors[1]. Several fields of applications, such as automation, communication, renewable energy storage and sensing are constantly unfolding, as semiconductors play a leading part in modern technology[1],[2]. The development of sensors and transducers has been rising throughout the years in the areas of automobiles, biomedical devices and environmental monitoring[3],[4]. Recent advances in the fields of micro- and nanofabrication have brought various types of sensors to the scientific forefront, such as electrical, chemical, electrochemical and optical amongst others[1],[5]. A widely used potentiometric electrochemical sensor is the ISFET (Ion-Sensitive Field-Effect Transistor) device.

An ISFET is virtually an extension of a MOSFET (Metal-Oxide Field-Effect Transistor) device where the metal gate has been replaced by a reference electrode immersed into an electrolyte solution[6], as shown in Figure 1.1. The basic principle of the device is that unscreened ion charges of the solution are mirrored to electrical charges into the semiconductor-oxide interface (channel) of the device, whose conductivity is controlled by applying a bias at the reference electrode[7]. In addition, the oxide-solution interface consisting of hydroxyl (-OH) groups renders the sensor to be pH-sensitive, whereas the specific detection of target species can be realized followed by the modification of the oxide with appropriate receptors[6].

The first ISFET device was introduced by Dr. Piet Bergveld in 1970 for ionic measurements in a neurophysiological environment[1],[8]. He additionally revealed its use for ion activities measurements in electrochem-

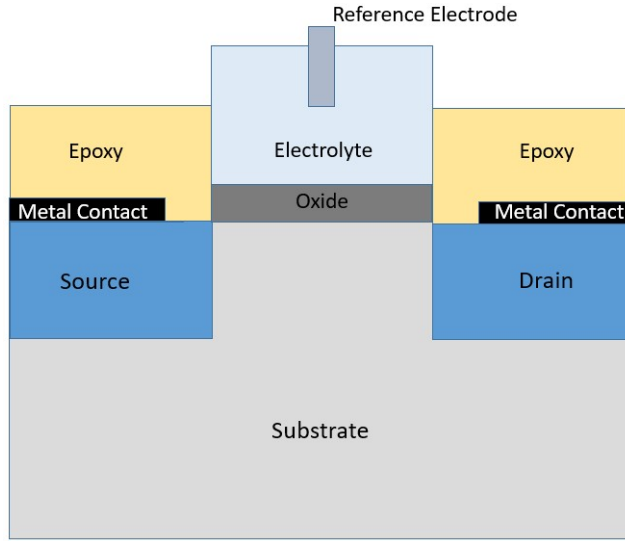


Figure 1.1: The substrate, the source, the drain and the gate oxide of an ISFET device, where the metal gate is replaced by a reference electrode immersed into the electrolyte solution. The epoxy is utilized to insulate the metal contacts and the wires from contact with the solution.

ical and biological environments[1]. Since their introduction, ISFETs have shown immense promise thanks to their numerous advantages, including sensitivity and selectivity, potential for miniaturization and large multiplexing capabilities[9],[10]. Furthermore, their real-time detection, label-free sensing, low power consumption, affordability and CMOS compatibility further enhance their appeal as a valuable tool for a wide range of applications and research areas[9],[10],[11].

However, despite all the above-mentioned merits of ISFETs, several challenges and limitations hinder their efficiency in pH- and biomolecule sensing. First of all, the sensitivity of the devices is limited by the theoretical maximum Nernstian sensitivity of 59.2 mV/pH , which represents the ideal performance of a pH sensor[9]. Moreover, ISFETs are susceptible to signal drift over time and hysteresis, phenomena that compromise the long-term stability and accuracy of the devices[9],[10]. Furthermore, in the case of biomolecule sensing, the performance of ISFETs is also obstructed by the nonlinear charge screening effect, which limits the detection of biomolecules in physiological salt conditions. Finally, ultrasensitive biomolecules detection in sub-nanomolar concentrations is challenging due to limited signal-to-noise ratio (SNR) of ISFET devices[9],[10],[11].

In the context of these challenges and limitations, several sensor designs

and structures have been investigated by the scientific community for pH- as well as biomolecule sensing, as presented below.

1.2 State-of-the-Art

Firstly, Dual-Gate ISFETs (DGFETs), which implement an additional back gate, have gained substantial attention thanks to their ability to overcome the Nernstian sensitivity. Huang *et al.*[12] proposed an innovative DGFET where the bottom poly-gate (PG) transistor was used for the sensing instead of the top “fluidic-gate” one (FG), which was grounded and comprised of a high-k dielectric, as shown in Figure 1.2. The surface potential change, formed at the top-gate, modulated the threshold voltage at the bottom PG transistor via capacitive coupling and the device exhibited a super-Nernstian sensitivity of 453 mV/pH . In addition, the drift was significantly reduced ($53x$) and the SNR was improved by $155x$ compared to the single top-gate operation[12].

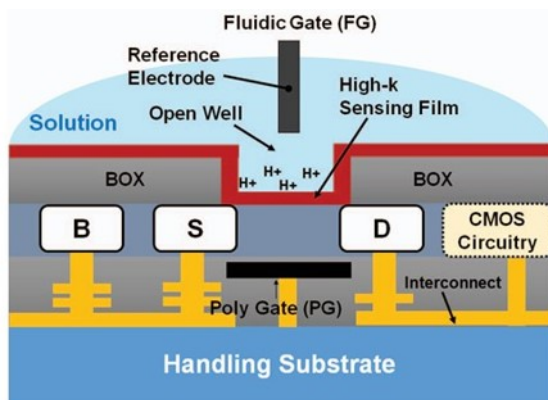


Figure 1.2: The DGFET device with the top high-k dielectric “fluidic”-gate (FG) and the bottom poly-gate (PG)[12].

Furthermore, regarding biomolecule sensing, an aptamer-modified carbon nanotube (CNT) FET was proposed by Maehashi *et al.*[13], for a label-free IgE detection with a limit of 47 nM at high salt concentration. Since aptamers are smaller in size than the Debye length, the binding between the target proteins and aptamers could take place within the electrical double layer in high salt, allowing the detection by the CNT-FET[13] and overcoming the nonlinear charge screening effect. In addition, Hideshima *et al.*[14], demonstrated a feasible strategy for the quantitative measurement of liver-tumor marker alpha-fetoprotein (AFP) in blood serum at a clinical

level, using an antibody-modified FET, where Bovine Serum Albumin (BSA) blocking was also implemented for minimizing the non-specific adsorption of blood proteins[14].

Morover, the multiplexing capabilities of ISFETs have also been investigated and exploited. In particular, Xu *et al.*[15] suggested an all-electrical multiplexed GFET DNA array where each FET acted not only as a sensing device but as an electrophoretic electrode as well, enabling a site-specific immobilization of probe DNA. The chip detected single-stranded DNA targets upon hybridization at maximum sensitivity of 100 fM at low salt concentration (0.005 x PBS)[15]. Finally, cytokeratin fragment 21-1 (CYFRA 21-1) and neuron-specific enolase (NSE), two lung-tumor markers, were simultaneously detected in blood serum by Cheng *et al.*[16] using an antibody-based multianalyte FET biosensor. The detection limits were 1 ng/mL for the CYFRA 21 – 1 and 10 ng/mL for the NSE biomarker.

Overall, biomolecule and protein detection is essential for comprehending vital functions in biological processes, studying diseases and developing personalized medicine. In this framework, the EU "ElectroMed" Project aims to advance precision medicine by creating a high-throughput peptide microarray technology capable of detecting proteins at low (nM) concentrations with high chemical variability. The core innovation of the project is a programmable instrument that integrates electrochemical peptide synthesis with nano-functionalized FET sensors within a microfluidic platform for parallel screening. The resulting prototype will synthesize specific peptide sequences for the *in situ* analysis of multiple target proteins at the same time, by implementing nano-functionalized FET arrays, thus exploiting the multiplexing capabilities of FETs. Ultimately, the final prototype will offer a faster, cheaper and more efficient protein detection compared to existing technologies and will assist the selection of neo-antigens for cancer vaccines based on exome-sequencing and mutational analysis.

1.3 Goals of the work

In the framework of the EU "ElectroMed" project, planar junctionless FETs were fabricated by Shukla *et al.*[17]. The goal of this Master Thesis was multifaceted and advanced towards the investigation of FETs suitability for the peptide synthesis monitoring via pH tracking as well as the detection of target biomolecules (Antibodies) with the prospective goal of studying their affinity to the peptide sequence; crucial steps for the implementation of nano-FETs onto the "ElectroMed" project. In particular, the Master Thesis project consisted of:

- The electrical characterization of devices in terms of pH sensing,
- The surface functionalization of devices with Boc protection and deprotection groups with the goal of investigating FETs suitability regarding the solid-phase peptide synthesis monitoring via pH tracking, and
- The surface modification of devices in order to explore their ability to detect Antibodies with the prospective goal of studying the biomolecules affinity to the grafted peptide sequence.

Overall, this Master Thesis project provided a significant insight regarding the ISFET devices abilities and limitations and contributed to a great extent towards the materialization of the "ElectroMed" project.

1.4 Report Overview

In Chapter 2, the theory required for the comprehension of the project is presented. In particular, the accumulation mode (IS)FETs, the pH response of ISFET devices, the solid-liquid interface by the Gouy-Chapman-Stern (GCS) model and the drift effect are described. Furthermore, since the goal of this project is the detection of biomolecules via the surface modification of the gate, a short introduction to biomolecules, solid-phase peptide synthesis and surface chemistry is outlined. Moreover, Chapter 3 consists of the Methods used within the scope of the project, where the chip encapsulation, the pH measurement setup, the surface functionalization and the Antibody detection experiments are presented. In Chapter 4, the experimental work regarding the pH characterization of the devices, their gate-surface modification and the Antibody experiments is described, while the results are analyzed and interpreted. Finally, Chapter 5 and 6 constitute the conclusion and outlook part, respectively, where a summary of the project is described and the future elaboration is reported.

Chapter 2

Theory

2.1 Field-Effect Transistors (FETs)

Field-Effect Transistors (FETs) consist of three terminals, namely the source, the drain and the gate, as shown in Figure 2.1. Typically, MOSFETs have a fourth terminal as well at the substrate. The source and drain contacts are highly conductive and separated by a channel. When an appropriate source-to-drain (V_{ds}) voltage is applied, current can flow from one terminal to the other (I_{ds}), providing that charge carriers are present in the channel. The presence of charge carriers, and thus the conductivity of the channel can be modified by the gate-to-source (V_{gs}) voltage. The gate is usually made of a metal or poly-silicon and it is separated from the channel by an oxide layer[6].

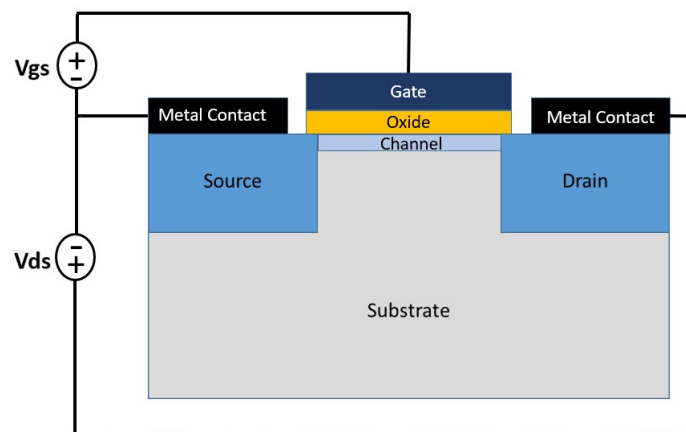


Figure 2.1: The Field-Effect Transistor consists of the source, the drain and the gate terminal. The gate is separated from the channel by an oxide layer.

2.2 Accumulation mode SOI FETs

2.2.1 SOI FETs

A modern generation of FETs are the Silicon-on-Insulator (SOI) transistors, which are comprised of a thin device layer, a buried oxide (BOX) and a thicker handle layer, as depicted in Figure 2.2. The advantages of SOI transistors compared to conventional bulk FETs are numerous, including lower parasitic capacitance, thanks to the presence of the BOX layer which yields an isolation of the device from the bulk and lower power consumption. Additionally, it is possible to fabricate devices, where the source and drain can have the same polarity with the body of the transistor[18],[19]. Such devices, like the p^+pp^+ ones that were used in the scope of this project, are called junctionless transistors.

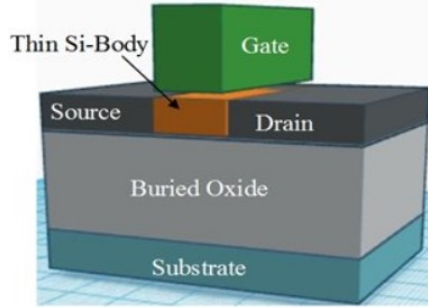


Figure 2.2: An SOI FET comprising of the thin device layer, the BOX layer and the substrate or handle layer[19].

Junctionless p^+pp^+ transistors are easier to fabricate since the need for pn junctions is eliminated and the requirement of doping concentration gradients is avoided. Thus, the horizontal and vertical electric fields are lower, providing lower leakage currents and significantly reduced short channel effects[18],[19]. The transistors can also operate in accumulation mode, without the need for the inversion of the device layer.

2.2.2 Accumulation-mode FETs

In accumulation mode, the threshold voltage ($V_{th,acc}$) at which a surface accumulation layer starts forming is the so-called flatband voltage (V_{fb}), which is given by:

$$V_{fb} = \phi_{ms} - \frac{Q'_{ox}}{C'_{ox}} = V_{th,acc} \quad (2.1)$$

where ϕ_{ms} is the difference between the work function potentials of the metal (ϕ_m) and the semiconductor (ϕ_s), Q'_{ox} is the effective interface charge per unit area within the oxide and C'_{ox} is the gate oxide capacitance per unit area[20]. The term "flatband voltage" has been derived by the fact that when this voltage is applied at the gate of the transistor, the energy bands at the side of the semiconductor are flat[21].

When the gate voltage (V_{gs}) is lower than the flatband voltage (*i.e.* greater in absolute value), the accumulation charge (holes) starts forming at the oxide-semiconductor interface (channel) of the device. By using the gradual channel approximation, *i.e.* voltages vary gradually along the channel from the source to the drain, the accumulation current can be given by[20]:

$$I_{acc} = \begin{cases} \frac{W}{L}\mu_s C'_{ox'}[(V_{gs} - V_{fb})V_{ds} - \frac{V_{ds}^2}{2}], & \text{if } V_{ds} > V_{gs} - V_{fb}. \\ \frac{W}{2L}\mu_s C'_{ox'}(V_{gs} - V_{fb})^2, & \text{if } V_{ds} < V_{gs} - V_{fb}. \end{cases} \quad (2.2)$$

where W , L are the width and length of the channel respectively, μ_s is the hole surface mobility and V_{ds} is the source-to-drain voltage.

Furthermore, in accumulation-mode FETs the bulk carriers can also contribute to the current, if there is a portion of non-depleted silicon under the channel. The width of the conduction bulk is modulated by the vertical extension of the front-gate depletion zone (assuming that the back gate does not contribute to the depletion depth, since the back gate was not utilized in the framework of this project)[20]. By solving Poisson's equation:

$$\frac{d^2\Phi(x)}{dx^2} = \frac{qN_A}{\epsilon_{Si}} \quad (2.3)$$

where $\Phi(x)$ is the potential along the depth of the device layer, $q = 1.6 \cdot 10^{-19}$ C is the unit charge, N_A is the acceptor atoms concentration and ϵ_{Si} is the electric permittivity of silicon, the front-gate depletion zone ($X_{depl}(y)$) is given by:

$$X_{depl}(y) = -\frac{\epsilon_{Si}}{C'_{ox'}} + \sqrt{\frac{\epsilon_{Si}^2}{C'^2_{ox'}} + \frac{2\epsilon_{Si}(V_{gs} - V_{fb} - V(y))}{qN_A}} \quad (2.4)$$

where $V(y)$ is the local potential along the channel.

If the front-gate depletion depth is greater than the device layer thickness (t_{Si}), then the film is fully depleted. The voltage (V_{depl}) with respect to the flatband voltage at which the whole body is depleted is:

$$V_{depl} = \frac{qN_A t_{Si}}{C_{ox'}} + \frac{qN_A t_{Si}^2}{2\epsilon_{Si}} \quad (2.5)$$

and when $V_{gs} > V_{fb} + V_{depl}$, the silicon device layer is fully depleted and no accumulation nor body current flows[20],[22].

By using again the gradual channel approximation for the body, the body current (I_{body}) can be given by:

$$I_{body} = \frac{W}{L} qN_A \mu_b A \quad (2.6)$$

where μ_b is the hole body mobility and the term A is a function of the applied biases and depends on whether the film is fully-depleted or not as well as whether the non-depleted film extends all the way from the source to the drain[20].

Overall, the body current ranges between the values of:

$$I_{body} \in [0, \frac{W}{L} qN_A \mu_b t_{eff} V_{ds}] \quad (2.7)$$

where the extreme values cases are shown in Figure 2.3 and t_{eff} is the effective device layer thickness ($t_{Si} - X_{depl}$). Comprehensively, the drain-to-source current (I_{DS}) is equal to:

$$I_{ds} = I_{acc} + I_{body} \quad (2.8)$$

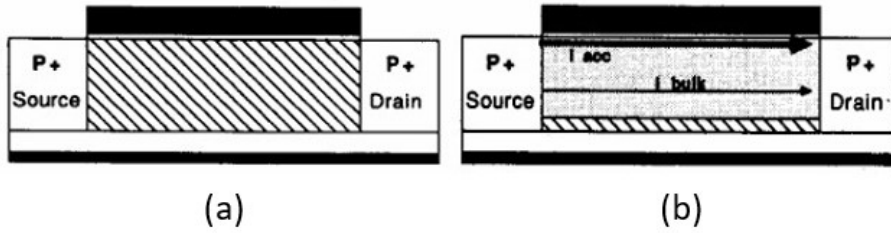


Figure 2.3: (a) The film is fully depleted and there is no accumulation nor body current flow, (b) The film is non-depleted and the accumulation layer extends from source to drain[19].

Typical $I_{ds} - V_{ds}$ and $I_{ds} - V_{gs}$ characteristics for a junctionless p+pp+ device are presented in Figure 2.4 and 2.5 respectively.

Finally, the transconductance (g_m) is a fundamental parameter that characterizes the efficiency of a FET device in converting the input gate voltage

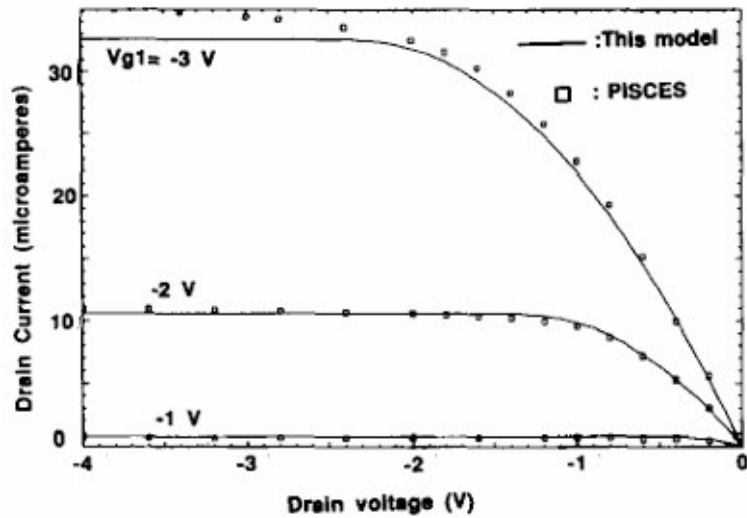


Figure 2.4: A typical $I_{ds} - V_{ds}$ characteristic of an accumulation-mode FET for different V_{gs} values. The solid line is analytical modeling and the squares are PISCES simulation results[19].

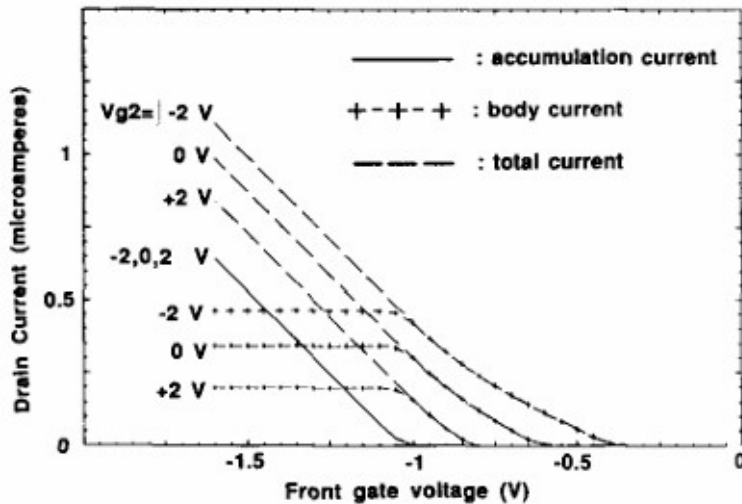


Figure 2.5: A typical $I_{ds} - V_{gs}$ characteristic for an accumulation-mode FET for different back-gate (V_{g2}) voltages. It can be seen that the total drain current is the superposition of the accumulation and the body current. The drain voltage is -100 mV . The intercept of the extension of the linear regions with the horizontal axis is approximately equal to the threshold voltage (V_{fb})[19].

into the output drain current and it is defined as the ratio of the drain current change (dI_{ds}) to the gate voltage change (dV_{gs}), while the drain voltage (V_{ds}) is constant, *i.e.*

$$g_m = \left. \frac{dI_{ds}}{dV_{gs}} \right|_{V_{ds}=\text{const.}} \quad (2.9)$$

The transconductance is desired to be high for a higher device efficiency and besides the applied biases dependence, it also depends on the physical parameters of the device, such as the carriers mobility (μ), the gate oxide capacitance, the width and the length of the device.

2.2.3 Accumulation-mode ISFETs

For an accumulation-mode ISFET, the above-mentioned equations are similar with the exception of the threshold voltage ($V_{th,ISFET}$). Two additional terms are incorporated into the threshold voltage, which is now given by:

$$V_{th,ISFET} = E_{REF} - \psi(pH) + \chi_{sol} + V_{fb,ISFET} \quad (2.10)$$

where E_{REF} is the reference electrode standard potential, $\psi(pH)$ is the potential drop across the electrolyte-insulator interface, χ_{sol} is the surface dipole potential of the solvent and $V_{fb,ISFET}$ is the flatband voltage of the ISFET device which is given by:

$$V_{fb,ISFET} = -\phi_s - \frac{Q'_{ox}}{C'_{ox}} \quad (2.11)$$

since there is no metal at the gate ($\phi_m = 0$). It can be seen that the surface potential $\psi(pH)$ is ion-sensitive and depends on the interaction of the target species with the oxide receptors[23].

2.3 pH theory

2.3.1 pH value

The first mathematical definition of pH was given by Søren Sørensen, stating that pH is the negative logarithm of the hydrogen ion concentration[27]:

$$pH = -\log[H^+] \quad (2.12)$$

While the pH scale extends to numbers below 0 and above 14, the range (0-14) is most commonly used. Plain water is considered to be neutral (pH

7), while acids have a pH value < 7 and bases a pH value > 7 . It should be noted that, in an aqueous solution, the hydrogen ion is not free, but rather bonded to a water molecule, thus forming the hydronium ion (H_3O^+).

Moreover, the pH value can also be derived by the dissociation constant of water K_w (10^{-14} at $25^\circ C$)[24]:

$$K_w = [H_3O^+][OH^-] \quad (2.13)$$

However, in an aqueous solution, organic and inorganic electrolytes are also present affecting the activity of the hydronium ions. As a result, a solution's acidity is determined by the activity and not the concentration of the hydronium ions, leading to the more accurate modified formula of pH[24]:

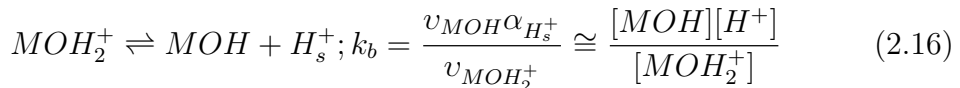
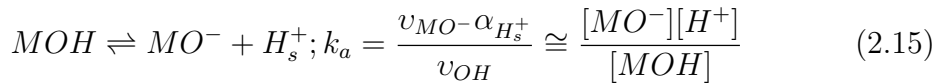
$$pH = -\log[a_{H^+}] \quad (2.14)$$

where a_{H^+} is the activity of hydrogen ions.

2.3.2 pH response of ISFETs

As already explained in Section (2.2.3), the surface potential developed at the oxide of an ISFET device is pH-dependent, rendering the ISFET device to be pH-sensitive. This behavior originates from the fact that oxides comprise of oxygen (O^-) atoms, which are defined as dangling bonds. Once the oxide is introduced into an aqueous solution, all the dangling bonds interact with a hydrogen (H^+) atom forming hydroxyl-(OH) sites on the oxide surface, which act as receptors. Furthermore, hydrogen ions of the solution can have a dynamic reaction with the surface, protonating and de-protonating the surface's OH sites. Therefore, the oxide's surface can contain neutral hydroxyl-sites (MOH) as well as protonated (MOH_2^+) or de-protonated (MO^-) ones, depending on the pH of the solution[6],[25].

This mechanism can be described by the site-binding model[25], where the surface reactions are:



where k_a , k_b are the dimensionless dissociation constants, v_i is the number of sites per area and $\alpha_{H_s^+}$ is the activity of the surface protons.

In addition, the total surface charge can be given by:

$$Q = q([MOH_2^+] - [MO^-]) \quad (2.17)$$

and assuming that the total density of available sites (N_s) is:

$$N_s = [MO^-] + [MOH] + [MOH_2^+] \quad (2.18)$$

it can be derived that, the total surface charge is:

$$Q = qN_s \frac{k_a k_b - [H_s^+]^2}{k_a k_b + k_b [H^+] + [H^+]^2} \quad (2.19)$$

Furthermore, by setting Equation (2.19) equal to zero, and by defining the pK_a and pK_b values:

$$pK_a = -\log(k_a) \quad (2.20)$$

$$pK_b = -\log(k_b) \quad (2.21)$$

the oxide's point of zero charge (p_{zo}) can be found, which is equal to:

$$P_{zo} = \frac{pK_a + pK_b}{2} \quad (2.22)$$

When the pH of the solution matches the point of zero charge, the net surface charge is going to be zero, since the number of (MOH_2^+) and (MO^-) will be equal (Figure 2.6a). On the other hand, if the pH is larger than the point of zero charge, the surface is going to be negatively charged, as the number of (MO^-) will be greater than the number of (MOH_2^+) (Figure 2.6b). Finally, when the pH is smaller than the point of zero charge, the net surface charge will be positive (Figure 2.6c)[6],[25],[26]. It should be noted that for silicon dioxide (SiO_2) the pK_a and pK_b values are 6 and -2 respectively, rendering its point of zero charge to be $p_{zo, SiO_2} = 2$.

However, due to the accumulation of charges at the surface, the concentration of hydrogen ions in the bulk [H_B^+] is different than that at the surface [H_s^+]. Their relation is given by the Boltzmann statistics:

$$[H_s^+] = [H_B^+] e^{-\frac{q\psi_0}{k_B T}} \quad (2.23)$$

where ψ_0 is the ion-sensitive surface potential, k_B is the Boltzmann constant and T is the temperature ($k_B T = 25.7 \text{ meV}$ at room temperature). This equation can be translated into the Nernst Equation:

$$pH_s = pH_B + \frac{q\psi_0}{2.3k_B T} \quad (2.24)$$

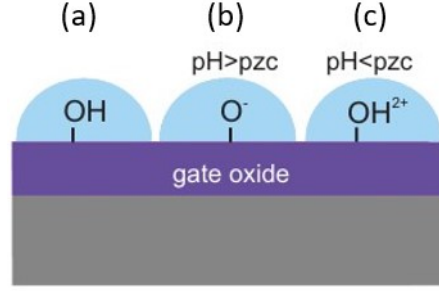


Figure 2.6: (a) If the pH of the solution matches the point of zero charge (p_{zo}), the net surface charge is going to be zero, (b) If the pH of the solution is greater than the point of zero charge, the majority of the surface sites are going to be de-protonated, (c) If the pH of the solution is less than then point of zero charge, the majority of the surface sites are going to be protonated[6].

which implies:

$$\psi_o = 2.3 \frac{k_B T}{q} (pH_s - pH_B) \quad (2.25)$$

By taking the partial derivative of the surface potential *w.r.t.* pH_s , it can be derived that:

$$\frac{d\psi_o}{dpH_s} = \frac{d\psi_o}{dpH_B + d\left(\frac{q\psi_o}{2.3k_B T}\right)} \quad (2.26)$$

and by using the chain rule:

$$\frac{d\psi_o}{dpH_s} = \frac{d\psi_o}{dQ} \frac{dQ}{dpH_s} \quad (2.27)$$

The first order of Equation (2.27) represents the reciprocal of the *double layer capacitance* (C_{dl}), which will be described in Section (2.4), while the second term is equal to $(-q\beta_{int})$, where β_{int} represents the change in the number of ionizable groups due to the change at the surface pH and is defined as the *intrinsic buffer capacity*, given by:

$$\beta_{int} = 2.3N_s \frac{k_b[H^+]^2 + 4k_a k_b[H^+] + k_a k_b^2}{(k_a k_b + k_b[H^+] + [H^+]^2)^2} [H^+] \quad (2.28)$$

Thus, Equation (2.27) can be re-arranged into:

$$\frac{d\psi_o}{dpH_s} = \frac{1}{C_{dl}} (-q\beta_{int}) \quad (2.29)$$

By combining Equations (2.26) and (2.29), the relation between the change at the surface potential due to the change at the bulk solution pH can be

given by:

$$\frac{d\psi_0}{dpH_B} = -2.3 \frac{k_B T}{q} \left(1 + \frac{2.3 k_B T C_{dl}}{q^2 \beta_{int}}\right)^{-1} = -2.3 \frac{k_B T}{q} \alpha \quad (2.30)$$

where $\alpha = \left(1 + \frac{2.3 k_B T C_{dl}}{q^2 \beta_{int}}\right)^{-1}$ is a dimensionless parameter ranging from 0 to 1, which depends on the double layer capacitance and the intrinsic buffer capacity. If $\alpha = 1$, then the ISFET device will have the maximum sensitivity of $59.2 \text{ mV}/pH$ known as the Nernstian sensitivity[25],[26].

It should be noted that a small difference between the surface pK points, namely $\Delta pK = \Delta pK_B - \Delta pK_a$ is desirable, since it maximizes the value of the intrinsic buffer capacity, which increases the value of α , improving the sensitivity. Moreover, it can also be seen that the double layer capacitance affects the sensitivity[1],[26].

Finally, a relation between the surface potential and the pH of the solution has also been derived by Bousse *et al.*[27] and is given by:

$$\psi_0 = 2.3 \frac{k_B T}{q} \frac{\beta}{\beta + 1} (p_{zo} - pH) \quad (2.31)$$

where β is a dimensionless parameter given by $\beta = \frac{2q^2 N_s \sqrt{k_a k_b}}{C_{dl} k_B T}$.

2.4 The solid-liquid interface - The Gouy-Chapman-Stern (GCS) model

As already presented in Section (2.3), once the oxide is introduced into an aqueous solution, the formed hydroxyl sites react dynamically with hydrogen ions and as a result they tend to protonate and de-protonate. The net surface charge created by the protonated and de-protonated hydroxyl- groups is neutralized by counter ions in the electrolyte via the formation of the so-called electrical double layer, as can be seen in Figure 2.7[1],[28]. Typically, the counter ions are surrounded by an aggregate of water molecules, which are electrostatically attracted by them and the Outer Helmholtz Plane (OHP) is defined by the locus of the counter-ions centers. Furthermore, a number of ions are "getting free" from the water molecules and they are specifically adsorbed onto the surface to a distance called the Inner Helmholtz Plane (IHP)[1],[25]. These two planes form the Stern layer, which is compact and where the potential drops linearly (Figure 2.8a).

The Stern layer can be seen as a capacitor C_H of value:

$$C_H = \frac{\epsilon \epsilon_0}{d} \quad (2.32)$$

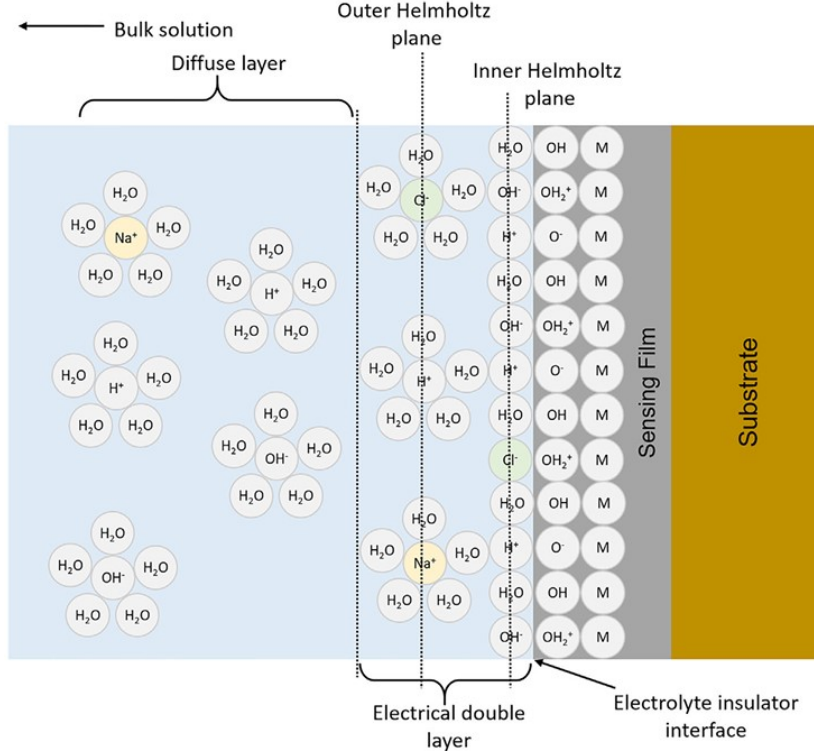


Figure 2.7: The solid-liquid interface described by the Gouy-Chapman-Stern (GCS) model[1].

where ϵ is the dielectric permittivity of the solution, $\epsilon_0 = 8.854 \cdot 10^{-12} \text{ F/m}$ the dielectric permittivity of free space and d the Stern layer thickness, usually close to 1 nm . Thus, the potential ψ_H at the end of the Stern layer is given by:

$$\psi_H = \psi_0 - \frac{\sigma_0 d}{\epsilon \epsilon_0} \quad (2.33)$$

where σ_0 is the surface charge and ψ_0 is the surface potential.

Moving from the Stern layer towards the electrically neutral bulk of the solution, there is the so-called diffuse or Gouy-Chapman layer, where the ions are not fixed, but they tend to diffuse due to thermal motion. By using Poisson's equation and Boltzmann statistics, it can be derived that the diffuse layer charge (σ_{DL}) (Figure 2.8b) is equal to:

$$\sigma_{DL} = -\sqrt{8k_B T \epsilon \epsilon_0 n^0} \cdot \sinh\left(\frac{zq\psi_H}{2k_B T}\right) \quad (2.34)$$

where n^0 , q and z are the concentration, the charge and the valence of each ion in the solution respectively, resulting in a diffuse layer capacitance (C_D)

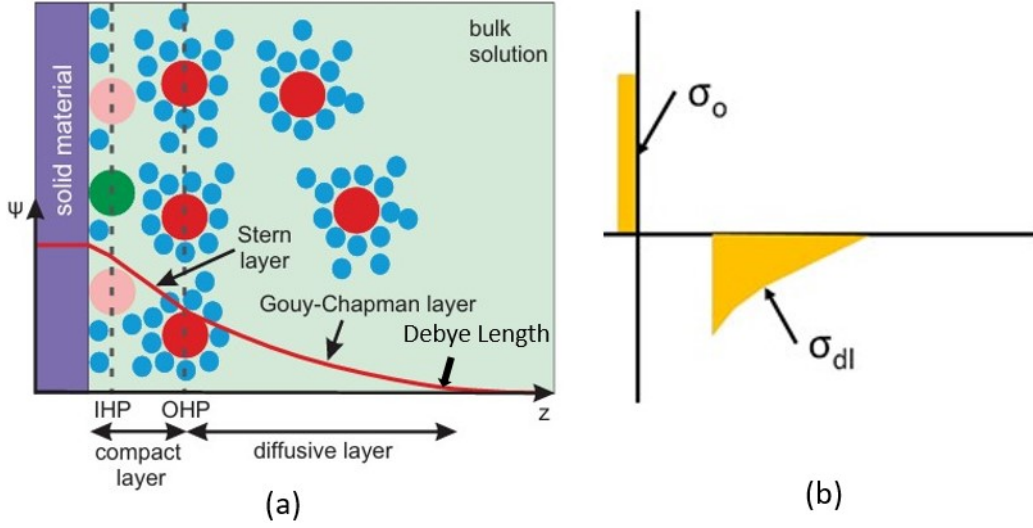


Figure 2.8: (a) The potential distribution of the electrical double layer, (b) The charge distribution of the electrical double layer[6].

of:

$$C_D = \sqrt{\frac{2z^2q^2\epsilon\epsilon_0n^0}{k_B T}} \cdot \cosh\left(\frac{zq\psi_H}{2k_B T}\right) \quad (2.35)$$

The distance to which the diffuse layer extends and the potential decays into the bulk solution is the diffuse layer thickness (κ) and the inverse of it is defined to be the so-called *Debye length* (λ_D) (Figure 2.8a) given by:

$$\lambda_D = \frac{1}{\kappa} = \sqrt{\frac{\epsilon\epsilon_0 k_B T}{2z^2q^2n^0}} \quad (2.36)$$

Overall, by defining the double-layer capacitance (C_{dl}) as the ability of the double-layer to store charge in response to a change in the surface potential:

$$C_{dl} = \frac{d\sigma_0}{d\psi_0} = -\frac{d\sigma_{dl}}{d\psi_0} \quad (2.37)$$

it can be derived that the total double-layer capacitance is the series combination of the Stern layer capacitance (C_H) and the diffuse layer one (C_D). Therefore, the double-layer capacitance (C_{dl}) can be given by:

$$\frac{1}{C_{dl}} = \frac{d}{\epsilon\epsilon_0} + \frac{1}{\sqrt{\frac{2z^2q^2\epsilon\epsilon_0n^0}{k_B T}} \cdot \cosh\left(\frac{zq\psi_H}{2k_B T}\right)} = \frac{1}{C_H} + \frac{1}{C_D} \quad (2.38)$$

In the case of immunoFETs or macromolecules detection in general, the Debye length is an important parameter, since it defines the sensing ability of the device. An ISFET device can only detect charge changes that occur within the Debye length and its sensitivity is reduced when the distance of the charges from the sensor surface is increased[28]. In immunoFETs, the Debye length can be monitored by the physiological salt solution concentration, where for 1x, 0.1x, 0.01x and 0.001x Phosphate Buffer Saline (PBS) at room temperature, the Debye length is 0.7, 2.3, 7.3 and 23 nm respectively[28].

2.5 Drift

ISFETs as well as related biosensors experience a secondary effect characterized by the temporal change in the threshold voltage when undergo a prolonged exposure to the electrolyte solution[29],[30]. Drift can lead to instability of the device by limiting its accuracy of measurements in time[29]. Besides the temporal change in the threshold voltage, drift can also be defined as the shift in the rate of change of the gate-to-source voltage under constant current. All sensing oxides experience drift with silicon dioxide (SiO_2) exhibiting the most considerable one compared to other sensing layers, such as Al_2O_3 , Ta_2O_5 , Si_3N_4 or HfO_2 [29].

Possible causes of drift can be the sodium ions (Na^+) migration inside the gate insulator due to the oxide field, negative space charges within the SiO_2 due to the injection of electrons from the electrolyte at strong anodic polymerization and the point of zero charge (p_{zo}) shift[30]. However, long term drift is mainly provoked by the diffusion of protons within the oxide layer and due to the electric field created by the ions' diffusion, as shown in Figure 2.9[29].

A mathematical model explaining the long term drift has been proposed by Hazarika *et al.*[29]. The diffusion of protons inside the oxide layer is a result of the concentration gradient. The electric field (E_{drift}) that develops within the oxide is equal to:

$$E_{drift} = \frac{qD_p}{\sigma} \frac{dP}{dx} \quad (2.39)$$

where $D_p = 9.3 \cdot 10^{-5} \text{ cm}^2\text{s}^{-1}$ is the protons diffusion coefficient, σ is the conductivity and P is the protons concentration. By differentiating and implementing Fick's Law of Diffusion:

$$\frac{dP}{dt} = -D_p \frac{d^2P}{dx^2} \quad (2.40)$$

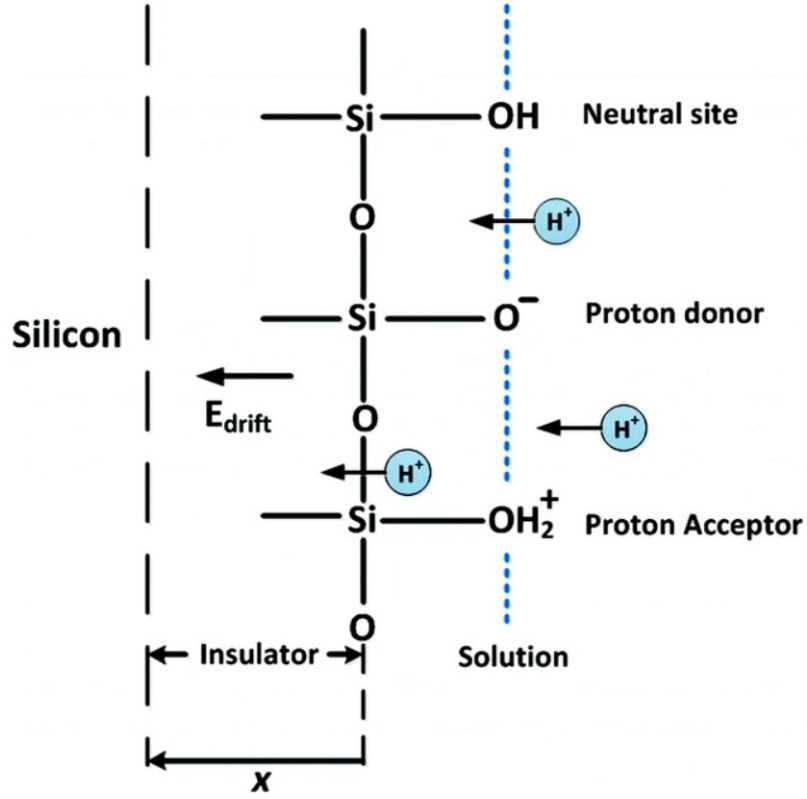


Figure 2.9: The diffusion of protons into the oxide and the electric field induced by it[29].

it can be derived that:

$$\frac{dE_{drift}}{dx} = -\frac{q}{\sigma} \frac{dP}{dt} \quad (2.41)$$

The time variant concentration P can be described by:

$$P = \frac{Q}{\sqrt{\pi D_p t}} e^{-\frac{x^2}{4D_p t}} \quad (2.42)$$

where Q is the surface concentration of protons. Since the dimension x is very small and the drift is observed for relatively long duration of time, it can be assumed that

$$x^2 \lll 4D_p t \quad (2.43)$$

Overall, the electric field caused by the diffusion of protons is given by:

$$E_{drift} = \frac{qQ}{2\sigma} \frac{1}{\sqrt{\pi D_p}} t^{-1.5} x \quad (2.44)$$

By integrating (2.44) *w.r.t.* distance x , the drift voltage (V_{drift}) can be given by:

$$V_{drift} = \frac{qQ}{4\sigma} \frac{1}{\sqrt{\pi D_p}} (t)^{-1.5} (x_j^2 - x_{ox}^2) \quad (2.45)$$

where x_{ox} is the oxide layer thickness and x_j is the distance travelled by the protons inside the oxide layer given by:

$$x_j = 2\sqrt{D_p t} \cdot \operatorname{erfc}^{-1}\left(\frac{C_{sensing}}{C_s}\right) \quad (2.46)$$

with $C_{sensing}$ and C_s being the trapped oxide charges and the surface charge respectively. Overall, the final threshold voltage if drift is considered ($V_{th(drift)}$) is given by:

$$V_{th(drift)} = V_{th,ISFET} - (V_{diffusion} + V_{drift}) \quad (2.47)$$

where

$$V_{diffusion} = \frac{q}{\psi_{ox}} (x_{ox} - 2\sqrt{D_p t} \cdot \operatorname{erfc}^{-1}\left(\frac{C_{sensing}}{C_s}\right)) \quad (2.48)$$

is the voltage developed due to the diffusion of protons within the oxide. Overall, the threshold voltage change due to the diffusion of protons is proportional to $t^{1/2}$, while due to the field caused by the diffusion is proportional to $t^{-3/2}$, yielding that the change due to diffusion is more dominant with the passage of time[29].

Furthermore, since long term drift is created by the penetration of H^+ ions into the oxide layer, it can be concluded that drift is more apparent at low pH, where the concentration of protons is higher[29],[30].

Strategies for minimizing and compensating for the drift effect can be the alternative sensor design, as the one discussed in the (1.2) Section, the use of correction algorithms[31] or the fabrication of the ISFET device using a different oxide material, such as HfO_2 , that is not porous and minimizes the penetration of protons within it.

2.6 Biomolecules

As already mentioned in Section (1.3), one of the goals of this project was the detection of Antibodies, while the general goal of the "ElectroMed" project consists of a peptide synthesis platform where the nano-functionalized FETs are implemented for protein detection. Subsequently, in this Section a short description regarding amino acids, peptides, solid-phase peptide synthesis and Antibodies is realized.

2.6.1 Amino Acids

Proteins are the most versatile macromolecules in nature serving numerous crucial functions in all biological processes[32]. They perform as catalysts, they provide mechanical support, they transport and store molecules, they transmit neural impulses and they control DNA replication[32],[33]. Proteins contain a vast range of functional groups and they are virtually polymers consisted of monomer units called *amino acids*[32].

Amino acids are organic compounds that share the exact same structure with each other: they consist of a central carbon atom, an amino group ($-NH_2$), a carboxylic acid group ($-COOH$), a hydrogen (H^+) atom and a distinctive "R" group, which is called the side chain, as shown in Figure 2.10a[32]. As ammonia ($-NH_3^+$) is a weaker acid than carboxylic acid, amino acids in equilibrium usually exist in the zwitterionic form, as shown in Figure 2.10b and depending on the pH of the solution, the amino and carboxylic groups are able to protonate and de-protonate.

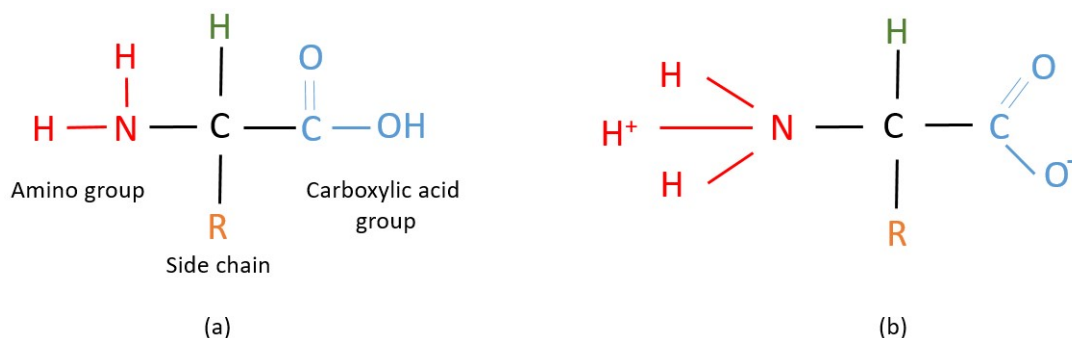


Figure 2.10: (a)The central carbon atom, the amino group, the carboxylic acid group, the hydrogen atom and the side chain of an amino acid, (b) The zwitterionic form of an amino acid.

All proteins found in species are constructed by the same set consisted of 20 amino acids. Each of the 20 amino acids has a different side chain group, which gives them variations in their functions and properties, such as size, shape, charge, hydrophobic character, chemical reactivity and hydrogen-bonding capacity[32].

2.6.2 Peptides

A *peptide* is a short linear chain of amino acids usually comprised of less than 10 amino acids, which are assembled together into a straight line, without featuring any branches[34]. The bond that allows this formation of amino

acids chains is the linkage of the carboxyl group of one amino acid to the amino group of another amino acid[32]. This bond is called the *peptide bond* and is accompanied by the loss of a water molecule, as shown in Figure 2.11. A series of amino acids formed together is called a *polypeptide chain* and each polypeptide chain has an amino group present at its one end and a carboxyl group at the other end. Each amino acid unit in a polypeptide chain is called a *residue* and by convention the amino end is considered to be the beginning of the polypeptide chain[32].

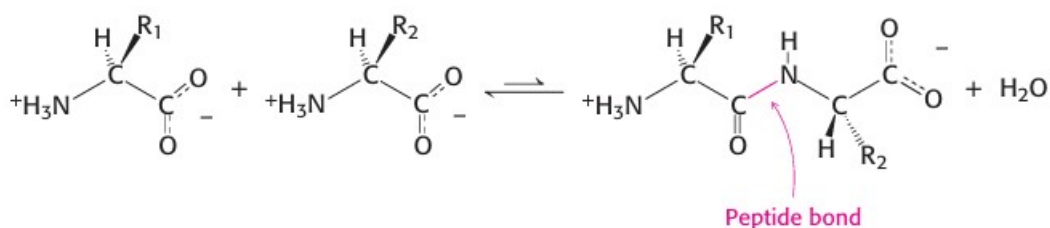


Figure 2.11: The linkage of two amino acids via the formation of a peptide bond and the loss of a water molecule[32].

2.6.3 Peptide Synthesis

Peptides of defined sequence can be synthesized via the solid-phase peptide synthesis (SPPS) method in order to assist in biochemical analysis[32]. Peptides of defined sequence are a valuable tool since they can serve as antigens for the formation of desired antibodies, they can isolate receptors for many signal molecules, such as hormones and they can also serve as drugs[32].

Since the amino groups of one amino acid is linked to the carboxyl group of another amino acid, a unique product is formed only if a single amino group and a single carboxyl group are available for the reaction. This can be accomplished by the blocking and activation of desired functional groups[32]. The SPPS method is illustrated in Figure 2.12. Firstly, the carboxyl-terminal residue is attached to an insoluble resin by its carboxyl group, acting as anchor and blocking it from peptide-bond-forming reactions (Figure 2.12a,b). The α -amino group of this amino acid is blocked with a protecting group, such as *tert*-butyloxycarbonyl (t-Boc), which will be described in the following section. This protecting group is removed with the use of an acid, such as *Trifluoroacetic Acid* (TFA)[32].

The next incoming amino acid in its t-Boc form is introduced along with a coupling agent, such as DCC (*Dicyclohexylcarbodiimide*). DCC reacts with the carboxyl group of the incoming amino acid, activating it for peptide-bond-forming reactions and removing a water molecule from the amino acids

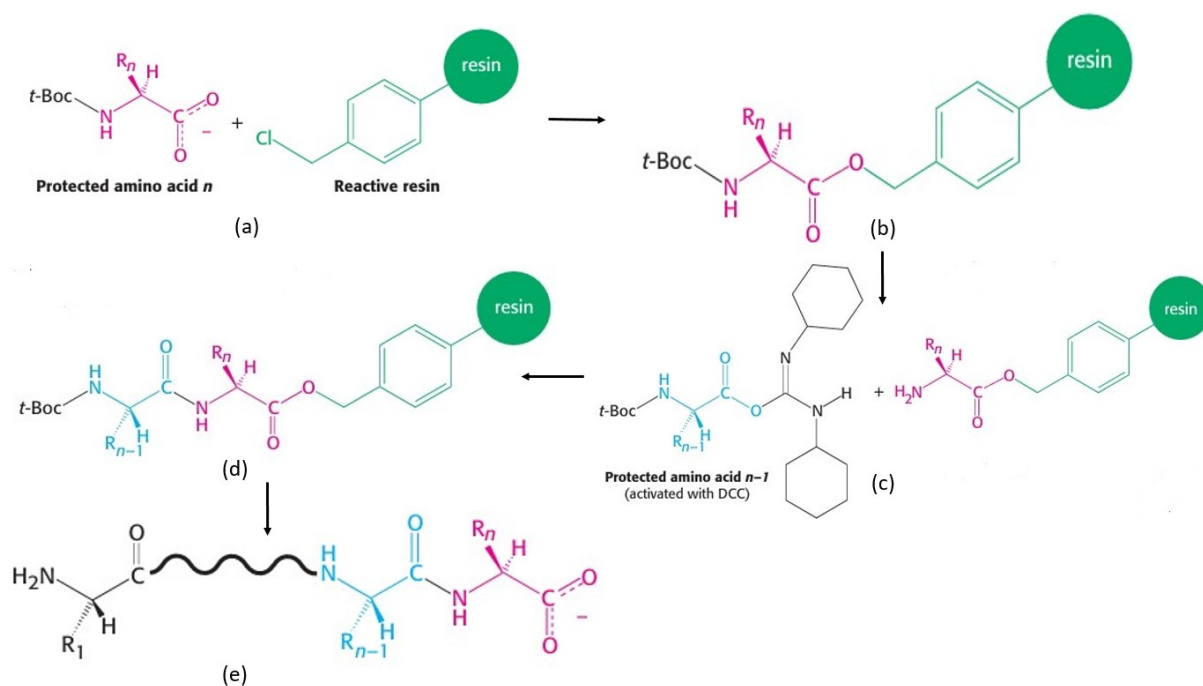


Figure 2.12: (a) The t-BoC protected amino acid and the resin, (b) The bonding of the resin to the t-BoC amino acid, (c) The t-BoC protected incoming amino acid activated with DCC and the de-protected amino acid, (d) The peptide bond formation, (e) The removal of the protection groups and the resin[32].

(Figure 2.12c,d). After the peptide bond has been formed, excess reagents are washed away and this procedure is repeated until the desired peptide sequence is obtained. When the synthesis is completed, the resin as well as potential protecting groups on the reactive side chains are removed with the use of *Hydrofluoric Acid* (HF) (Figure 2.12e)[32].

2.6.4 Antibodies

An *antibody* (also called an immunoglobulin, Ig) is a large y-shaped protein of weight approximately 150 *kDa* and size of about 10 *nm*, which is synthesized by a complex living organism in response to a foreign substance, called an antigen[32]. Four separate polypeptide chains form an antibody, which consists of two heavy and two light chains linked by disulfide bonds, as shown in Figure 2.13[32].

The heavy and light chains form the F_{ab} domains, which have the antigen-binding site at their ends. Each antibody has two identical F_{ab} domains, re-

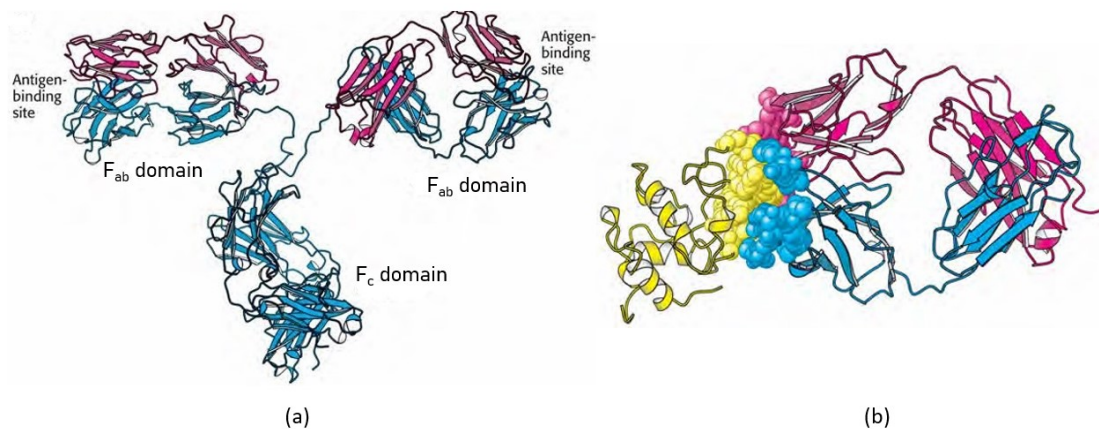


Figure 2.13: (a) The structure of an antibody consisting of four chains, two heavy (blue) and two light (red) ones, the F_{ab} and F_c domains and the antigen-binding sites, (b) The specific binding of an antigen to an antibody[32].

sulting in the binding of two antigens per antibody. Antibodies have specific and high affinity for the antigens that elicited their synthesis and the binding between the two serves as a protection tool of the immune system[32]. An antibody recognizes a specific group of amino acids on the target antigen, called the *epitope* and the specificity is a result of the complementary structures between the two surfaces (Figure 2.13b)[32].

On the other hand, the two heavy chains form the F_c domain, which is identical among all antibodies of the same immunoglobulin class and allows the binding of complement proteins[32].

2.7 Surface functionalization

2.7.1 APTES

Surface functionalization, or gate functionalization in the scope of this project, is an approach of altering a material's surface properties in order to become sensitive to specific target analytes or inhibit potentially undesired reactions[34]. In the case of oxide substrates, which have an abundance of hydroxyl (-OH) groups, silanization is usually the first step of functionalization and *3-aminopropyltriethoxysilane* (APTES) is the most popular choice used for it as it enables further binding of molecules thanks to its amine terminal[35].

APTES ($pK_a = 9$, $pK_b = 3.6$) is an aminosilane, consisting of three

ethoxy groups and one amino group per silane molecule, as shown in Figure 2.14a. The polymerization of an APTES molecule to an oxide substrate is a two-step process, consisting of the hydrolysis and the condensation reactions[36]. During hydrolysis, water molecules attack the ethoxy groups forming silanol (-SiOH) ones (Figure 2.14b). As soon as the first silanol groups have been formed, the condensation process begins in parallel with the hydrolysis. During condensation, the silanol groups of an APTES molecule can either react with the hydroxylated oxide surface or with the silanol group of another APTES molecule forming siloxane bonds (Si-O-Si), as illustrated in Figure 2.14c and 2.15[36].

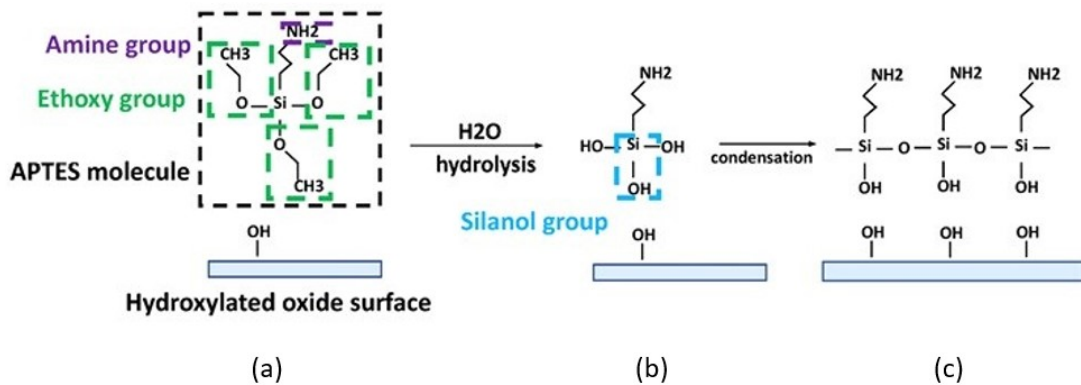


Figure 2.14: (a) The APTES molecule and the hydroxylated oxide surface, (b) The silanol group (-SiOH) formed after hydrolysis, (c) The formation of siloxane bond (Si-O-Si) between two APTES molecules[36].

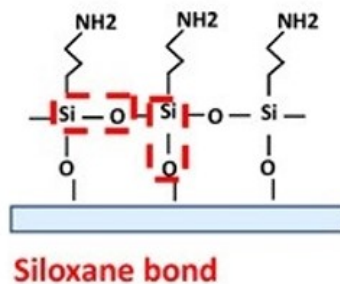


Figure 2.15: The formation of siloxane bonds between APTES molecule and the substrate[36].

In the presence of excess water molecules, the silanol groups of different silane molecules can react with each other, forming undesired polymeric

structures[36]. Therefore, an anhydrous solvent is often preferred in order to produce a more uniform monolayer deposition[35]. In that case, the hydrolysis step is performed by the hydroxyl groups on the oxide surface which attacks the ethoxy groups leading to the cleavage of the Si-O bond in APTES and the formation of silanol groups on the surface.

Besides the solvent type, various parameters can affect the reactions, such as the environmental humidity, the pH, the reaction temperature and time, the silane concentration as well as the pre- and the post-treatment of the surface[36].

2.7.2 Boc Protecting Groups

As discussed in Section (2.6.3), during peptide synthesis, specific groups of amino acids need to be protected in order to be non-reactive with other functional groups. For the protection of amino acids and amines, the most widely used protecting groups are carbamates, which can be placed and removed under relatively mild conditions[37]. One of the most commonly used carbamate for the amine protection is the *t*-butyloxycarbonyl (Boc) group, as illustrated in Figure 2.16a.

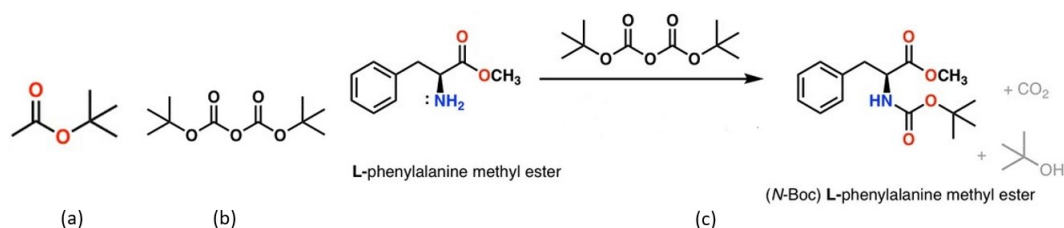


Figure 2.16: (a) The *t*-butyloxycarbonyl (Boc) protecting group, (b) The anhydride Boc_2O , (c) The protection of L-phenylalanine methyl ester into (N-Boc) L-phenylalanine methyl ester and the by-products of the reaction[37].

The formation of Boc-protected amines and amino acids can be conducted under aqueous or anhydrous conditions via the reaction of the anhydride *di-tert-butyl dicarbonate* (Boc_2O) (Figure 2.16b) with a base. The by-products of this reaction are *carbon dioxide* (CO_2) and a *t-butyl alcohol*, as presented in Figure 2.16c.

The removal of the Boc-protecting groups is conducted under acidic conditions. The most widely used acid for the Boc de-protection is the *Trifluoroacetic Acid* (TFA), which is illustrated in Figure 2.17a [37]. Similarly to

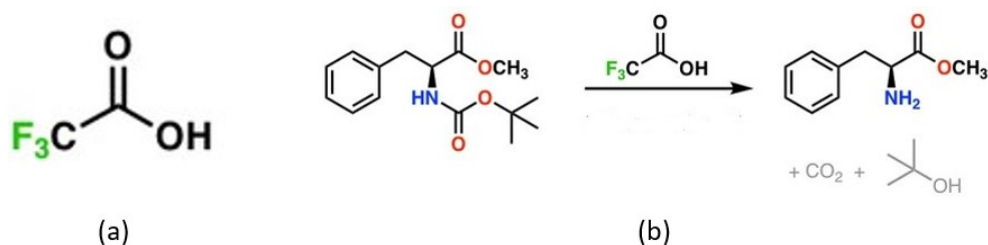


Figure 2.17: (a) The Trifluoroacetic acid (TFA), (b) The de-protection of (N-Boc) L-phenylalanine methyl ester to L-phenylalanine methyl ester[37].

the Boc-protection, the by-products of the Boc de-protection are CO_2 and a *t*-butyl alcohol (Figure 2.17b).

The Boc protection and de-protection reactions are presented in more detail in Figure 2.18 and 2.19 respectively.

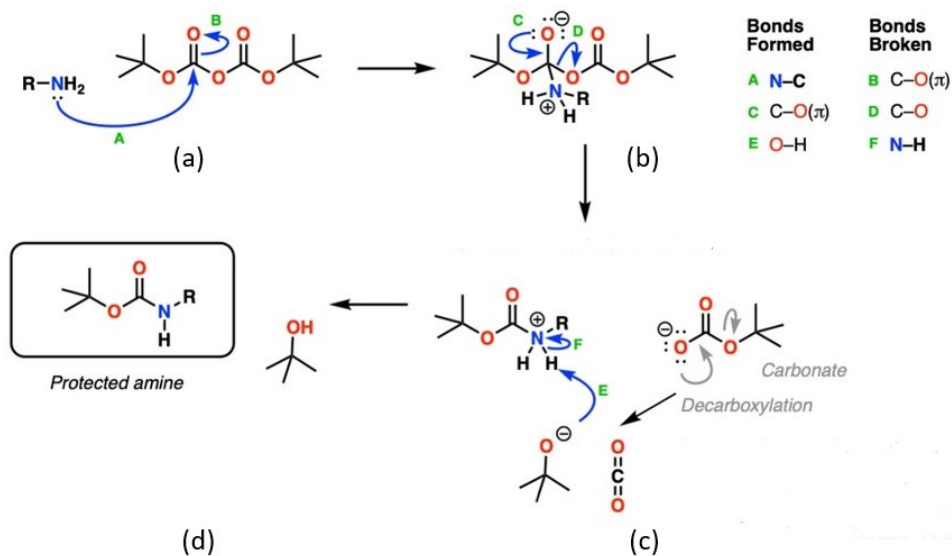


Figure 2.18: (a) The amine attacks the carbonyl atom of the carbonate, (b) The loss of a carbonate due to the elimination of oxygen, (c) The base needed for the reaction can be the carbonate which will decarboxylate producing CO_2 or the *t*-butoxide which is formed after the decarboxylation of the carbonate, (d) The protonated carbamate is neutralized and the amine is protected[37].

Chapter 3

Methods

3.1 pH Buffers

For the pH titration experiments, buffer solutions were prepared. Specifically, 0.1M Monobasic Potassium Phosphate (KH_2PO_4), Boric Acid (H_3BO_3) and Citric Acid ($C_6H_8O_7$) solution with 0.1M Potassium Nitrate (KNO_3) electrolyte were used as the initial testing solution of pH ~ 2.5 . During the experiments, 1M Potassium Hydroxide (KOH) solution of pH ~ 13.5 was introduced to increase the pH of the testing solution and perform a pH sweep measurement in the 2.5 - 10 pH range. All chemical compounds were purchased from Sigma-Aldrich.

3.2 Chip encapsulation

Chips were designed and fabricated by Shukla *et.al*[20]. The dimension of a single chip is $1 \times 1 \text{ cm}^2$, consisting of three SU-8 microfluidic channels and 14 aluminium contact pads. Overall, there are 12 junctionless SiO_2 -gate FET devices per chip along with a common-source and a pseudo-reference electrode, as illustrated in Figure 3.1a,b,c[17]. Diced chips were wire-bonded to a PCB for electrical connections using a 7440E Ultrasonic Wire Bonder. Following this, a two-component epoxy glue was used to insulate the metal contacts and the wires from contact with the solution. The chip was heated on a hot plate for $\sim 2h$, for proper insulation and hardening of the glue. Upon encapsulation, chips were blown with nitrogen (N_2) gas and stored in a N_2 box. The encapsulated chip is shown in Figure 3.1d.

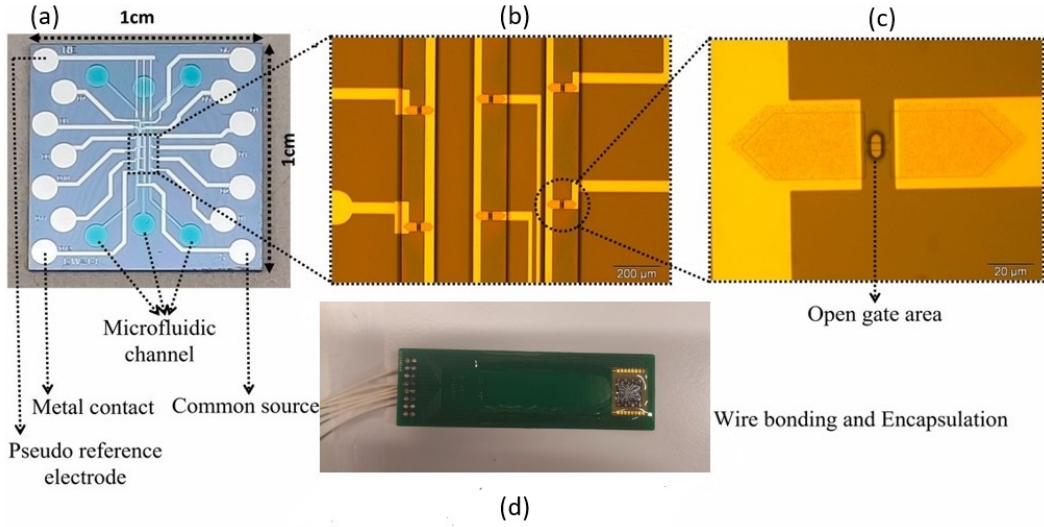


Figure 3.1: (a) A single chip, (b) The SU-8 microfluidic channels and the FETs, (c) The open-gate area of a FET device, (d) The wire-bonded and encapsulated chip on the PCB[17].

3.3 pH Measurement Setup

The encapsulated device was submerged in a vial containing a 40 mL solution consisting of 20 mL KH_2PO_4 , H_3BO_3 and $C_6H_8O_7$ and 20 mL KNO_3 solutions along with a reference electrode (REF201, red-rod saturated 3M KCl solution, Radiometer Analytical) connected to the power supply (Keithley 2410 SourceMeter) and a pH electrode connected to the pH meter (Seven-Multi S-400 Basic, Mettler Toledo). The initial pH was ~ 2.5 . The vial was placed on top of a magnetic stirrer and the solution was constantly mixed during the measurements. The drain contact was also connected to a second power supply (Keithley 2410 SourceMeter) and both the source contact and the two power supply devices were common-grounded. The whole setup was placed within a Faraday cage to shield any undesired interference and the experiments were conducted under darkness to limit the photocurrent activity.

Upon pH stabilization, the drain-to-source current (I_{ds}) and the gate-to-source current (I_{gs}) were recorded as a function of the applied biases, namely the drain-to-source voltage (V_{ds}) and the gate-to-source voltage (V_{gs}). Overall, four I-V curves were simultaneously recorded, namely $I_{ds} - V_{ds}$, $I_{ds} - V_{gs}$, $I_{gs} - V_{ds}$ and $I_{gs} - V_{gs}$ for the given pH. Using the I_{ds} characteristics, the working point of the devices was established and pH characterization measurements were conducted for devices that exhibited a low leakage current

($I_{gs} \sim 3$ orders of magnitude lower than I_{ds}).

Following the I-V recording, *KOH* solution of appropriate volume was added to the vial for the pH titration. The base solution was added by a syringe pump (Pump 11 Pico Plus, Harvard Apparatus) followed by the pH measurement and the I-V recording anew ($V_{ds} = 0.1$ V, -1 V $\leq V_{gs} \leq 0.2$ V) until pH ~ 10 .

Overall, the process was fully automated with the use of a custom-built automated setup and controlled by a LabVIEW software (Figure 3.2), developed by Dmytro Shavlovskiy, Researcher at the University of Twente. The $I_{ds} - V_{gs}$ characteristics for the complete pH sweep and the pH-sensitivity ($V_{gs} - \text{pH}$) curves were plotted using Matlab.

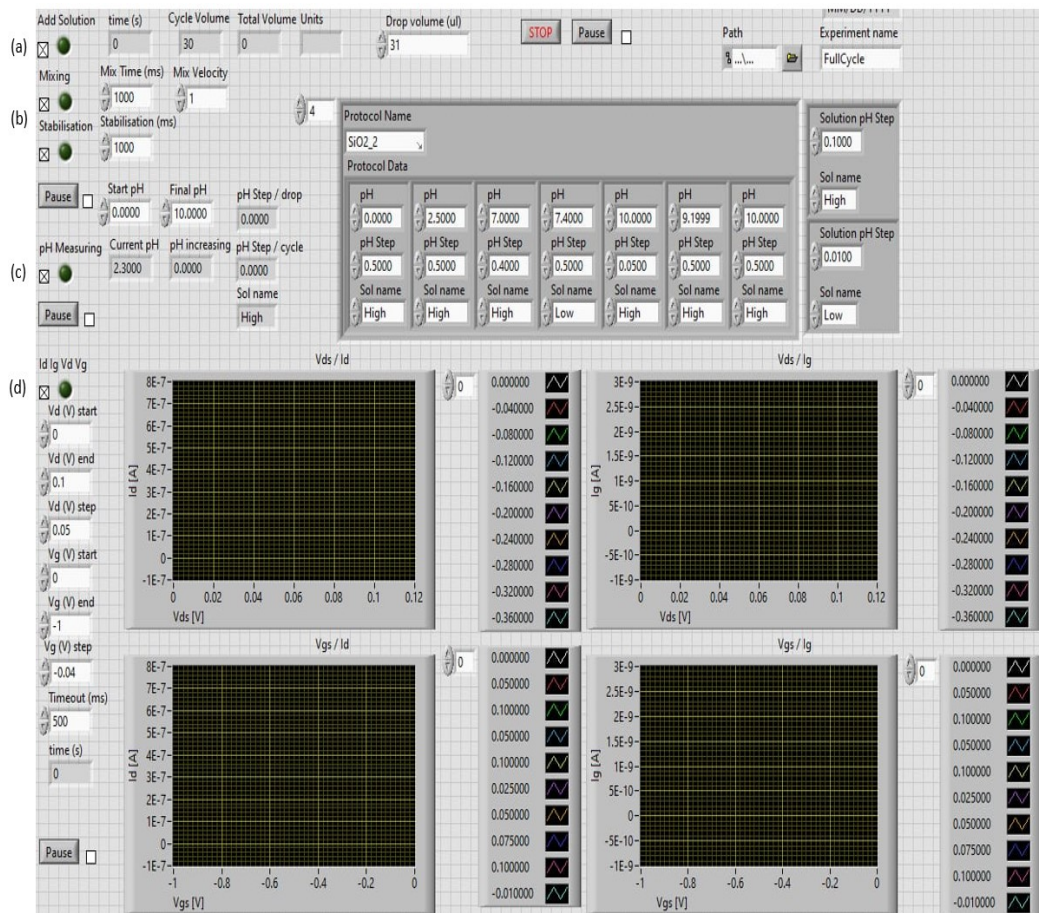


Figure 3.2: Upon establishment of the working point, a measurement cycle consists of (a) Adding of *KOH* solution with the use of the syringe pump, (b) Mixing and stabilization of the pH, (c) Registration of the current pH value, (d) I-V characteristics recording.

3.4 Surface functionalization

The 3-Aminopropyltriethoxysilane (APTES), the *N,N*-Diisopropylethylamine (DIEA), the Benzotriazol-1-yloxytripyrrolidinophosphonium hexafluorophosphate (PyBOP), the Trifluoroacetic Acid (TFA), the 3-Maleimidopropionic Acid *N*-Succinimidyl Ester (SMP), the Anti-Flag Antibody[®], the Polyethylene Glycol-7 (PEG-7) as well as the Absolute Ethanol (EtOH), the Acetonitrile (ACN), the Dimethyl Sulfoxide (DMSO) and the Phosphate Buffered Saline (PBS) tablets that were used for the surface functionalization of FETs were purchased from Sigma-Aldrich. The Boc-12-Acid-OH that was utilized for the Boc protection was purchased from Iris Biotech. The "DYKGGGSH" peptide was synthesized and sent from the ElectroMed partners in Luxembourg.

3.4.1 APTES

Prior to APTES functionalization, devices were activated in a *UV-O₃* cleaner for 30 min. Following this, chips were submerged into a 5% APTES in EtOH solution and heated at 50°C overnight covered by aluminium foil to prevent evaporation. Upon functionalization, devices were washed with EtOH and blow dried with *N₂* gas before conducting I-V measurements (Figure 3.3b).

3.4.2 Surface functionalization for pH-sensing

3.4.2.1 Boc / DeBoc

For the Boc functionalization, a solution of 150 mg Boc-Acid (Figure 3.4a), 248 μ L DIEA (Figure 3.4b), 742 mg PyBOP (Figure 3.4c) and 7.5 mL ACN was prepared and stirred for 15 min. The DIEA was utilized as the base required for the Boc-reaction, while the PyBOP was used as a coupling reagent for the control and acceleration of it. Lastly, the ACN was the organic solvent used for the reaction. The prepared solution was drop-casted on top of the open-gate area of the chips, which was covered with aluminium foil to avoid evaporation and the chips were left at room temperature for 1 h. Subsequently, the devices were cleaned with ACN and DI water and blow dried with *N₂* gas, before conducting I-V measurements (Figure 3.3c).

For the Boc de-protection, a 50% TFA in ACN solution was prepared and drop-casted at the open-gate area of the chips. The devices were again covered with aluminium foil and left at room temperature for 1 h. Upon functionalization, chips were washed with *KOH* for 5min to neutralize any excess reagents accompanied by a DI-water wash and blow dry with *N₂* gas,

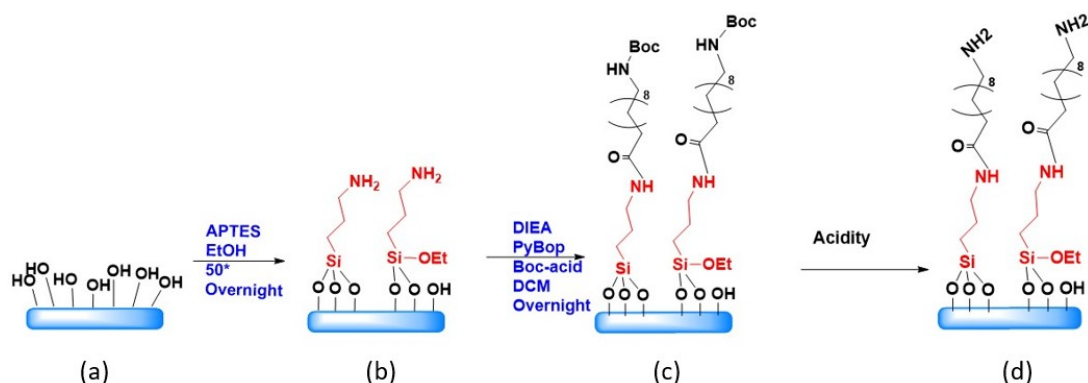


Figure 3.3: (a) The hydroxylated oxide surface, (b) The APTES-functionalized surface, (c) The Boc-Acid functionalized surface, (d) The de-protected surface.

before conducting I-V measurements (Figure 3.3d).

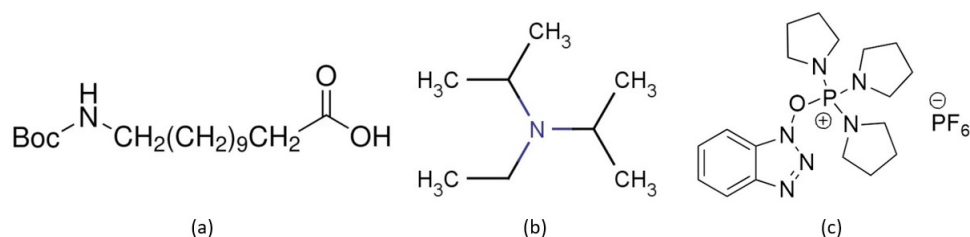


Figure 3.4: (a) The Boc-Acid[38], (b) The DIEA[39], (c) The PyBOP[40] used for the Boc protection.

3.4.3 Surface functionalization for Antibody detection

3.4.3.1 Ester

For the Antibody detection, the functionalization of the APTES surface with SMP (Figure 3.5) was realized. SMP is an amine-reactive heterobifunctional crosslinking reagent, widely used for the investigation of biomolecules interactions, as its two maleimide groups facilitate the covalent bonding between the APTES amine and the amino side chains of the target molecules, such as peptides[41].

A solution of 1 mg SMP in 2 mL DMSO was prepared and drop-casted on the sensor, which was covered with aluminium foil and left at room temperature for 3 h. Subsequently, the device was cleaned with DMSO and blow dried with N_2 gas, before I-V measurements were conducted (Figure 3.6c).

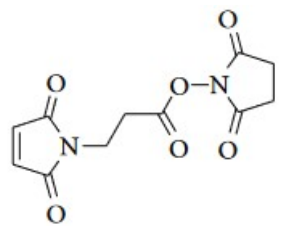


Figure 3.5: The *3-Maleimidopropionic acid N-succinimidyl ester* (SMP)[41].

3.4.3.2 "DYKGGGSH" peptide

The next step before the Antibody detection was the addition of a Flag-peptide layer and the grafting occurred by drop-casting a solution of 1 mg of "DYKGGGSH" peptide in 2 mL PBS into the chip's open-gate area. The device was again covered with aluminium foil and left at room temperature for 3 h (Figure 3.6d) followed by DI-water wash.

The choice for the specific peptide sequence was done based on the fact that the "DYK" ("Aspartic Acid - Tyrosine - Lysine") part is a biologically active peptide and specific to the Ab we desired to detect. Furthermore, the "GGGSH" ("Glycine - Glycine - Glycine - Serine - Histidine") sequence was selected as it is a relatively short linker, allowing the binding of the Ab close to the sensor's surface but avoiding its interaction with the bottom of the surface at the same time. Moreover, the "SH" part can interact with the maleimide group of the SMP, rendering the Ab detection feasible.

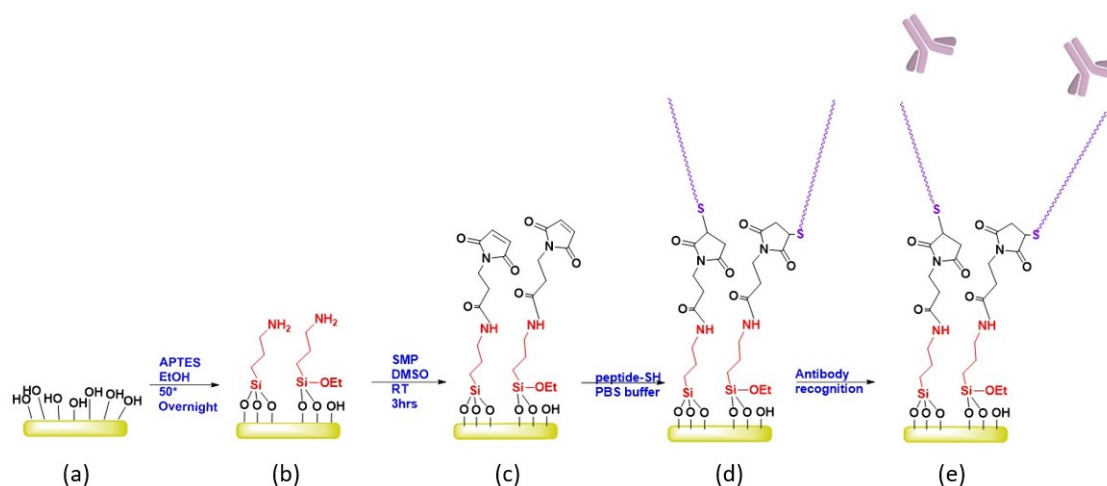


Figure 3.6: (a) The hydroxylated oxide surface, (b) The APTES-functionalized surface, (c) The ester-functionalized surface, (d) The binding of the peptide to the maleimide group of the SMP, (e) Antibody binding

3.4.4 Antibody detection

Upon surface functionalization with the SMP linker and the "DYKGGGSH" peptide, the sensors were examined for Antibody detection. The Anti-Flag Antibody® was chosen, as it is specific for the "DYK" part of the peptide and three solutions of different Ab concentrations (25 nM, 600 nM and 2.6 μ M in 0.01 x PBS) were prepared in order to examine the sensitivity of the sensors in the 0.2 nM - 100 nM concentration range. As already explained in Section (2.4), since Abs are long molecules, the choice of 0.01 x PBS was made in order to increase the Debye Length (~ 7.3 nm compared to ~ 0.7 nm of the 1 x PBS). Consequently, the biomolecules binding would take place inside the Debye length and the charge changes would be mirrored into the FET channel.

For the Antibody experiment, a smaller flexible reference electrode (Dri-Ref, World Precision Instruments) was placed on the open SU-8 area of the chips and connected to the power supply (Keithley 2410 SourceMeter). The drain contact was also connected to a second power supply and both the source contact and the two power supply devices were again common-grounded. Firstly, the working point of the sensors was established through the I-V characteristics and chosen in the region where the gate-voltage dependence of the drain current was linear ($V_{gs} = -0.6V$, $V_{ds} = 0.1V$).

Subsequently, the drain current was recorded for ~ 15 min in order to be stabilized of drift and for devices that exhibited drift even after this stabilization period, the drift was removed by signal processing in Matlab. Upon drain current stabilization, Antibodies were introduced using a pipette onto the surface of the chips for the following concentrations (0.2 nM, 0.5 nM, 1 nM, 2 nM, 3 nM, 4 nM, 5 nM, 6 nM, 7 nM, 8 nM, 9 nM, 10 nM, 11 nM, 12 nM, 13 nM, 20 nM, 50 nM and 100 nM). Before each Antibody concentration introduction, the drain current was recorded until stabilization.

3.4.5 Negative control

In order to perform a negative control experiment, following the SMP functionalization, chips were functionalized with PEG-7 ($H-(O-CH_2-CH_2)_7-OH$). PEGs are biocompatible and hydrophilic polyether compounds, whose synthesis is done by polymerizing ethylene oxide (C_2H_4O) and they are widely used for the blocking of biomolecules binding. The functionalization was done by drop-casting a solution of 1 mg of PEG-7 in 2 mL PBS into the chip's open gate area. The devices were covered with aluminium foil and left at room temperature for 3 h followed by DI-water wash.

Similar to the positive control experiment, the drain current was recorded

for ~ 15 min and Antibodies were introduced with the use of a pipette onto the open-gate area of the chips at the following concentrations (0.2 nM, 0.5 nM, 1 nM, 2 nM, 5 nM, 10 nM, 20 nM, 50 nM, 100 nM, 200 nM and 500 nM). Before each Antibody concentration introduction, the drain current was recorded until stabilization.

Chapter 4

Results

4.1 Experiments Overview

In the scope of the Master Thesis project, a series of experiments were conducted for the investigation of FETs as potential tools for the "ElectroMed" project requirements. In particular, based on the fact that pH measurements are the key tool for the *in situ* validation of surface modifications, devices were characterized in terms of voltage sensitivity *w.r.t.* pH, in order to examine their suitability towards this goal. Firstly, the pH sensitivity of bare SiO_2 -gate FETs was analyzed (Section 4.2) followed by the pH-sensitivity measurements and comparison of the APTES, Boc protected and Boc deprotected gate-surface (Section 4.3.1, 4.3.2). The reason behind the selection of the above-mentioned surface chemistry is the desire for the monitoring of the peptide synthesis procedure with the use of FETs.

Furthermore, given the fact that sensing target proteins utilizing nano-FETs is one of the main goals of the "ElectroMed" project, surface chemistry (APTES, SMP, "DYKGGGSH" peptide) was also implemented for Antibodies detection experiments. The I-V characteristics were recorded between each functionalization step (Section 4.3.3) and the experiment of Antibodies sensing was conducted (Section 4.4). Finally, having successfully detected Antibodies, the blocking of the biomolecules binding was also examined by performing a negative control experiment following the FETs functionalization with PEG-7 (Section 4.5).

4.2 pH characterization

The working point of the devices with channel width $W = 12 \mu\text{m}$ and length $L = 4 \mu\text{m}$ was derived by the measurement of the $I_{ds} - V_{ds}$ and $I_{ds} - V_{gs}$ char-

acteristics at $\text{pH} \sim 2.5$, as explained in Section (3.3). These characteristics provided that the working point of the junctionless FETs was $V_{ds} = 0.1$ V and $V_{gs} = -0.3$ V.

Subsequently, with the goal of characterizing the devices in terms of the voltage sensitivity *w.r.t.* pH, the $I_{ds} - V_{gs}$ characteristics were recorded over the 2.5 - 10 pH range for a gate-to-source voltage (V_{gs}) of 0.2 V to -1 V applied via the reference electrode and a drain voltage (V_{ds}) of 0.1 V, with the results illustrated in Figure 4.1.

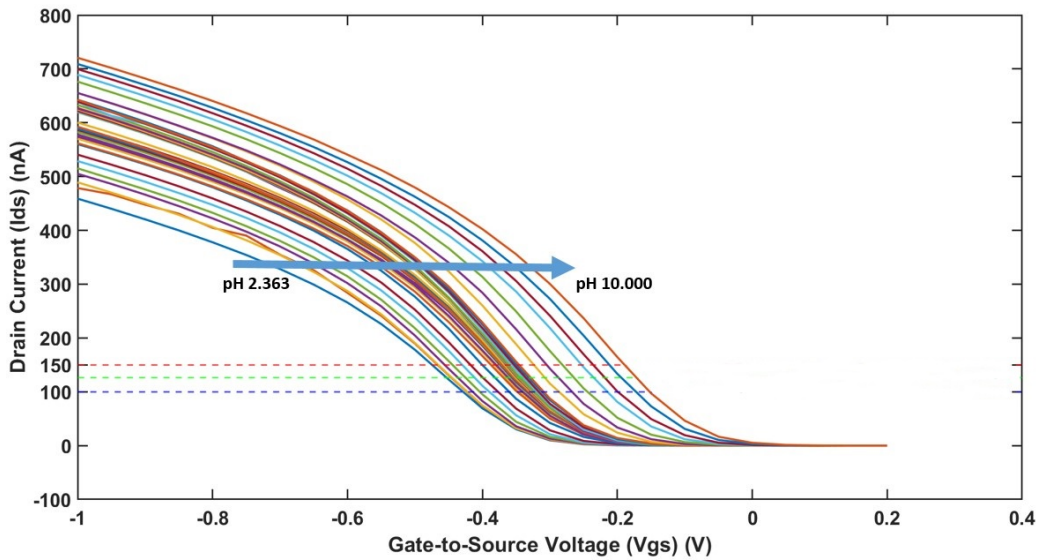


Figure 4.1: The $I_{ds} - V_{gs}$ characteristics for an applied V_{gs} ranging from 0.2 to -1 V and $V_{ds} = 0.1$ V over the $\sim 2.5 - 10$ pH range. The pH steps were 0.01 around the pK_a point (pH 5.9 - 6.1), 0.1 at the (5.5 - 5.9) and (6.1 - 6.5) pH ranges and 0.5 at the rest of the examined range. The chosen constant drain current values (100 nA, 125 nA, 150 nA) and their interpolation to the $I_{ds} - V_{gs}$ characteristics are illustrated as dotted lines.

It can be seen that, the drain current is approximately null around 0 V, until reaching the threshold voltage. Furthermore, it has a linear dependence on the gate voltage in strong accumulation, as it is expected for a FET device. However, at gate voltages less than -0.4 V ($V_{gs} < -0.4$ V) this linear dependence is replaced by the nonlinear behavior of I_{ds} *w.r.t.* V_{gs} (drop in the transconductance g_m). While this behavior is evident in p-channel devices due to mobility degradation effects, this is probably not applied here because the effect is not apparent for the same gate voltage range after the surface functionalization of the device, as it will be seen in the following Section. It is believed that this behavior could be originating from potential trapped

charges on the oxide due to fabrication processes, which are removed upon the conduction of I-V measurements, or due to some potential cracking of the SU-8 layer which increases the exposed width of the device, thus increasing the drain current.

As the pH increases the threshold voltage ($V_{th,ISFET}$) increases as well (becomes less negative) and the channel reaches at accumulation faster. This can be explained by the fact that at a higher pH more OH^- ions are present in the solution and de-protonate the oxide surface, changing the surface potential. Negative charges at the surface are mirrored into positive charges (holes) into the channel, leading the device to accumulation mode with lower applied gate voltages. Overall, the change in V_{gs} (through the shift in $V_{th,ISFET}$) due to a pH change indicates that the sensor is pH-sensitive.

By choosing a constant drain current value (I_{dtrg}), as shown in Figure 4.1, which ensures that the ISFET is in the linear region and interpolating the $I_{ds} - V_{gs}$ characteristic, the pH-sensitivity can be derived and calculated by applying a linear fitting. As can be illustrated in Figure 4.2, the sensitivity of the devices is $35.3 \pm 0.5 \text{ mV/pH}$, $35.7 \pm 0.3 \text{ mV/pH}$ and $36.2 \pm 0.3 \text{ mV/pH}$ for constant drain currents of 100 nA , 125 nA and 150 nA respectively.

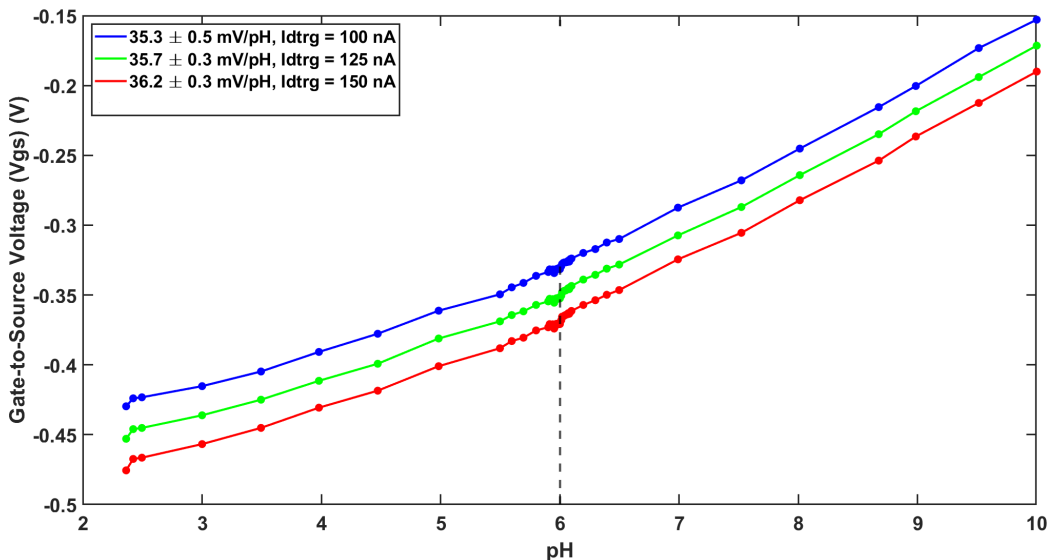


Figure 4.2: The calculated pH-sensitivity of the device for three drain current values (I_{dtrg}), namely 100 nA , 125 nA and 150 nA and the indicated $pK_a = 6$ point.

By zooming into the area around the pK_a point of SiO_2 ($pK_a = 6$) for the three plots above, it can be observed that the voltage change becomes more apparent right at the pK_a point (Figure 4.3). This can be explained by the

fact that the pH-sensitivity of the device is greater at the pK points because the intrinsic buffer capacity (Equation 2.28) maximizes improving the sensitivity. Moreover, it can be observed that the pH-sensitivity plot (Figure 4.2) exhibits a non-linear behavior around that point, due to transition between protonated and de-protonated states.

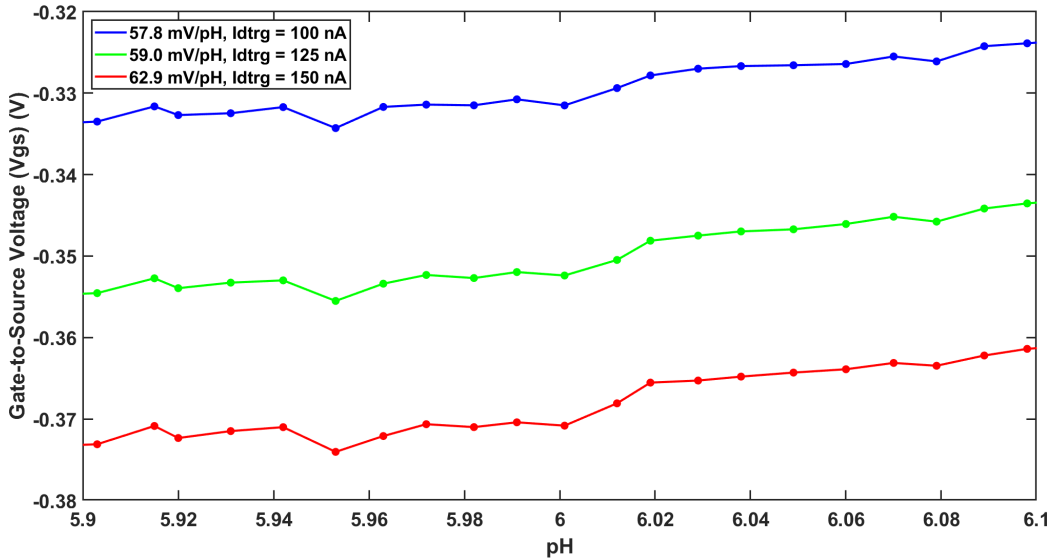


Figure 4.3: The gate-to-source voltage (V_{gs}) *w.r.t.* pH for the indicated drain current values (I_{dtrg}) around the $pK_a = 6$ point and the corresponding pH-sensitivities.

4.3 Surface functionalization

4.3.1 APTES

Following the APTES functionalization, the devices were characterized anew in the 2.5 - 10 pH range, with V_{gs} ranging from 0.2 V to -0.8 V and $V_{ds} = 0.1$ V. Figure 4.4 illustrates the $I_{ds} - V_{gs}$ characteristics at pH 7 for both the SiO_2 and the APTES surface. While the linear dependence of the drain current to the gate voltage stops at around $V_{gs} = -0.45$ V for the oxide, as described in the previous Section, this does not occur for the APTES-functionalized surface, where the linearity extends up to $V_{gs} = -0.8$ V.

Furthermore, it can be seen that the threshold voltage for the APTES surface is smaller (more negative) compared to the threshold voltage of the oxide. Based on the pK points of APTES ($pK_b = 3.6$, $pK_a = 9$), its amine

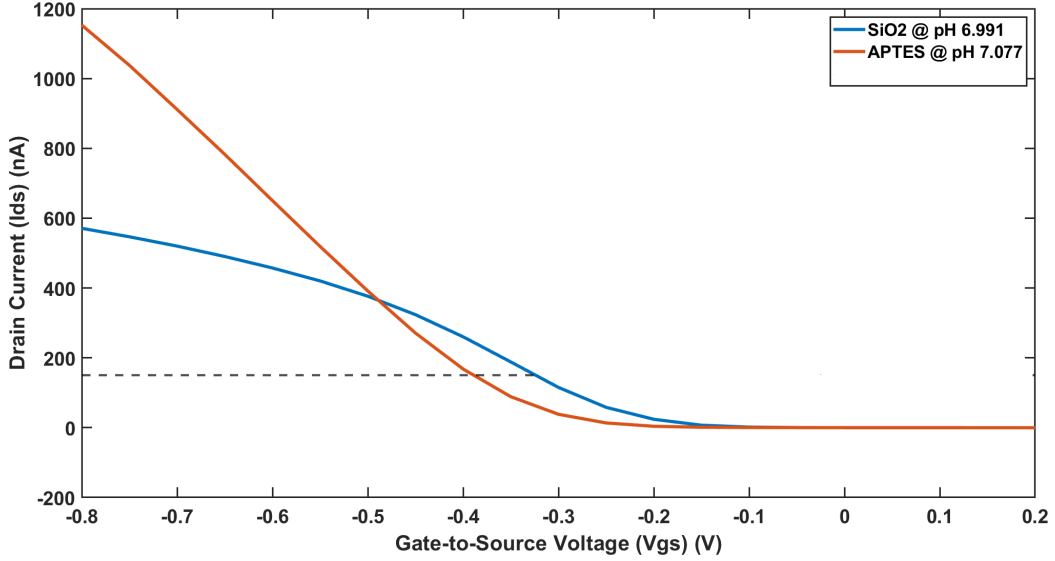


Figure 4.4: The $I_{ds} - V_{gs}$ characteristics for the SiO_2 and the APTES-functionalized surface at pH 7. The constant drain current ($I_{dtrg} = 150 \text{ nA}$) chosen for the interpolation is illustrated as a dotted line.

groups ($-NH_2$) are slightly de-protonated (NH^-) at a neutral pH environment. However, at the given pH, the SiO_2 surface is going to be highly de-protonated, which signifies the presence of more positive charge on the APTES surface compared to the SiO_2 . As a result, this positive charge is translated to less holes in the ISFET channel, rendering it harder for the channel to turn on and shifting the threshold voltage to more negative V_{gs} . Moreover, it is expected that the drain current of the oxide would be higher than that of the APTES surface, unless the linearity of the former one would cease.

By choosing again a current value where the two characteristics are linear and parallel (namely $I_{dtrg} = 150 \text{ nA}$, Figure 4.4) and interpolating the two characteristics, the pH-sensitivity can be derived, as shown in Figure 4.5. As already explained in Section (2.3.2), a small difference between the surface pK points increases the value of the intrinsic buffer capacity, thus increasing the value of α and improving the sensitivity. Consequently, the pH sensitivity for the APTES surface ($41.0 \pm 1.4 \text{ mV/pH}$) is improved compared to the bare SiO_2 .

In addition, around the pK points of APTES, a non-linear behavior is exhibited, similar to the bare SiO_2 ($pK_a = 6$).

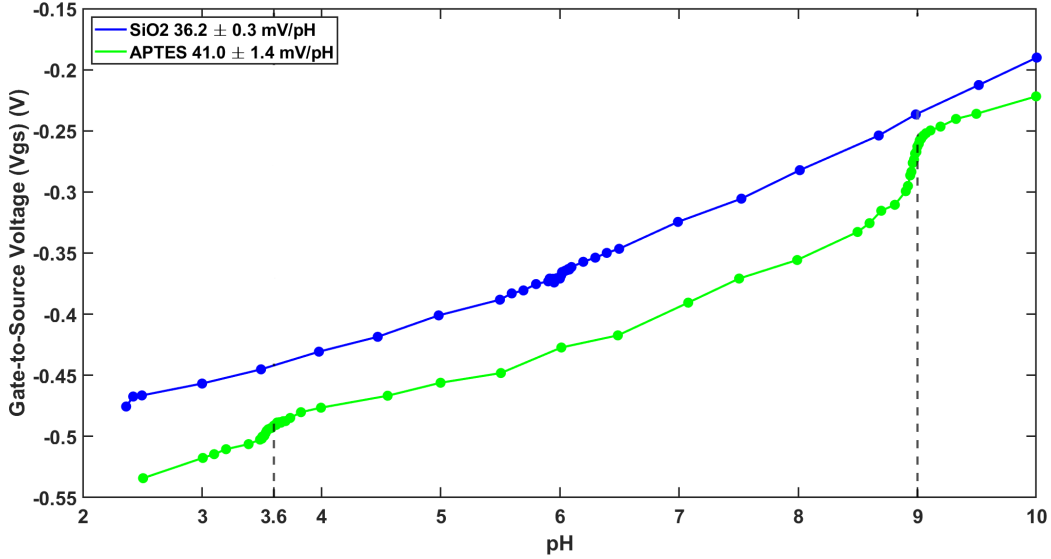


Figure 4.5: The pH-sensitivity for the bare SiO_2 and the APTES-functionalized surface for $I_{dtrg} = 150nA$ and the indicated APTES $pK_b = 3.6$ and $pK_a = 9$ points.

4.3.2 Surface functionalization for pH-sensing

4.3.2.1 Boc / DeBoc

As already mentioned, the Boc protection surface chemistry is essential for the *in situ* monitoring of the peptide synthesis process. As described in Section (2.6.3), during peptide synthesis specific functional groups of amino acids are Boc-covered for their reaction to be blocked and once the desired peptide bond is formed, the protecting groups are removed (DeBoc). Based on this, following the APTES functionalization, the devices were functionalized with Boc-Acid (Section 3.4.2) and characterized at the same voltage and pH range. In order to track the Boc/DeBoc quality, the Boc-Acid functionalized devices were subsequently de-protected (Figure 3.3) and the chips were characterized once more.

The $I_{ds} - V_{gs}$ characteristics for the four surfaces are illustrated in Figure 4.6. In the case of the Boc protected surface, the surface is still sensitive to voltage changes, explaining the drain current behavior. However, the exact form of the characteristic (threshold voltage, drain current value) cannot be fully interpreted, as non-specific binding of protons into a potential bare part of SiO_2 or uncovered APTES molecules can affect the parameters. Nevertheless, from Figure 4.7 it can be observed that, the Boc-protected surface exhibits almost no sensitivity in the (2.5 - 4.5) pH range, while the overall

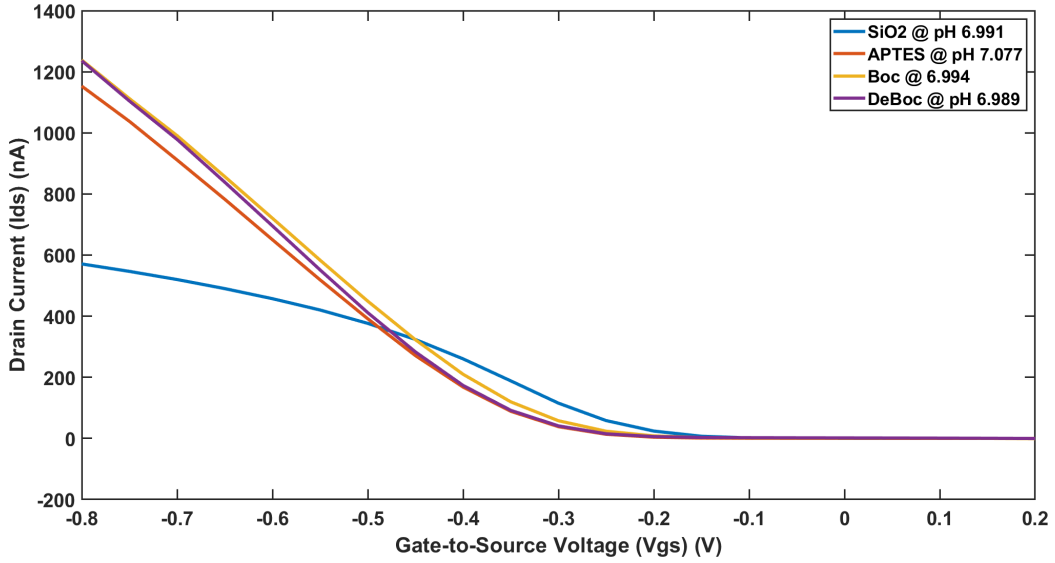


Figure 4.6: The $I_{ds} - V_{gs}$ characteristics for the SiO_2 , the APTES functionalized surface, the Boc protected surface and the Boc de-protected (DeBoc) surface at pH 7.

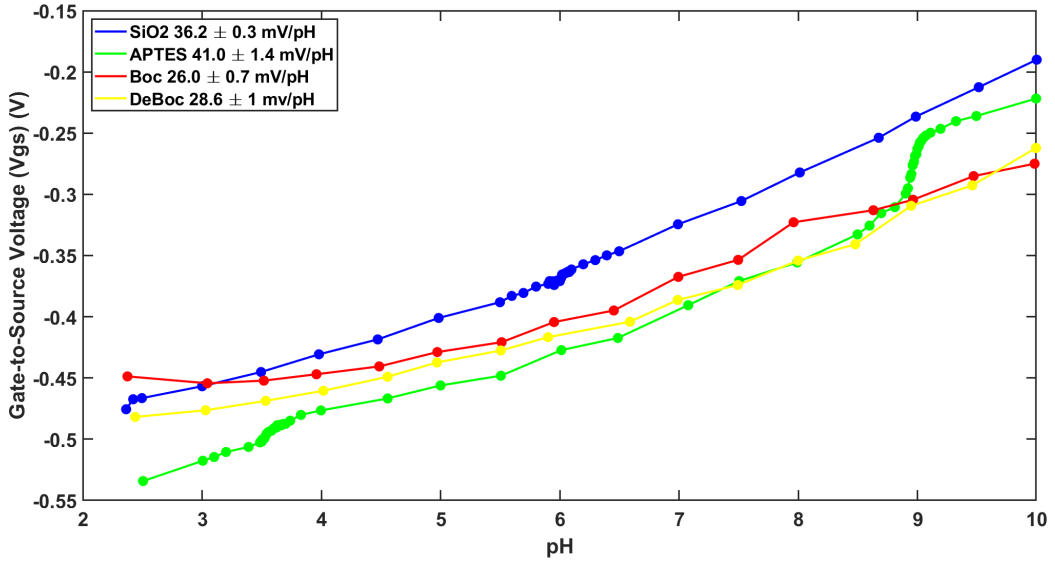


Figure 4.7: The pH-sensitivity for the bare SiO_2 the APTES functionalized surface, the Boc protected and the Boc de-protected (DeBoc) surface for $I_{dtrg} = 150nA$.

pH-sensitivity has greatly reduced to $26.0 \pm 0.7 mV/pH$ compared to the APTES sensitivity of $41.0 \pm 1.4 mV/pH$. Consequently, it can be concluded

that the Boc-protection was successful to a great extent.

Moreover, upon Boc de-protection, the amine groups of the Boc-Acid are revealed, resulting in a surface similar to the APTES-functionalized one. Based on this, the $I_{ds} - V_{gs}$ characteristics as well as the pH-sensitivity would be expected close to the APTES behavior. However, it can be seen that this is realized up to an extent, since the characteristic converge to the Boc one at higher gate voltages (Figure 4.6). Furthermore, the pH sensitivity of the DeBoc surface in the (2.5 - 4.5) pH range has been restored, while at high pH values (*e.g.* 8.5 - 10), it can be seen that the Boc de-protected surface is more sensitive than the Boc one (Figure 4.7). Overall, the pH-sensitivity is slightly improved ($28.6 \pm 1 \text{ mV/pH}$) compared to the Boc surface ($26.0 \pm 0.7 \text{ mV/pH}$). This indicates that a part of the Boc protecting groups were probably not uncovered by the de-protection.

Finally, it should be mentioned that Boc protection is a reversible reaction, suggesting that Boc protecting groups can be once more grafted on the de-protected amine groups (Figure 3.3d), by using Boc_2O along with a base solution. This was also attempted during the experiments, but with no significant results, because amine groups were not completely uncovered by the de-protection, as explained above.

Overall, based on the fact that chips are designed to monitor the Boc protection and Boc de-protection of the peptides during the solid-phase peptide synthesis, it can be concluded that the FETs could be suitable for this application. The quality of the Boc/DeBoc surface coatings could be accomplished via the pH sensitivity tracking upon each peptide synthesis step.

4.3.3 Surface functionalization for Antibody detection

Following the peptide synthesis, the next goal of the ISFET devices is the *in situ* detection of target proteins and biomolecules. Towards this goal, chips were modified with an appropriate surface chemistry and Antibodies detection experiments were conducted.

4.3.3.1 SMP - "DYKGGGSH" peptide

Upon APTES functionalization, chips with channel width $W = 4 \mu\text{m}$ and length $L = 4 \mu\text{m}$ were functionalized further with the SMP linker and the Flag-"DYKGGGSH" peptide. After each functionalization step, the I-V characteristics were recorded for data consistency and the results are shown in Figure 4.8 at pH 7.

For these chips, I-V measurements were not performed for the bare SiO_2 surface. This can explain the APTES behavior, where the transconductance

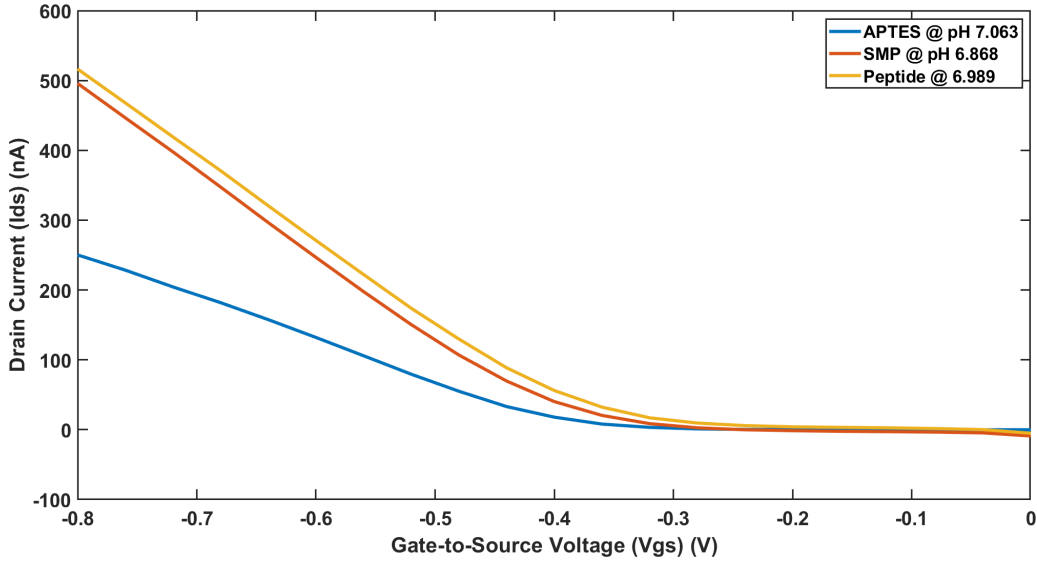


Figure 4.8: The $I_{ds} - V_{gs}$ characteristic of the sensor upon APTES, SMP (Ester) and peptide functionalization at pH 7.

drops after $V_{gs} \sim -0.45$ V, similar to the SiO_2 case of Figure 4.4. Furthermore, upon grafting on the sensor surface, the SMP linker is quite rigid and cannot be easily protonated and de-protonated. In addition, the isoelectric point of the "DYKGGGSH" peptide can be calculated to be at \sim pH 8, indicating that the peptide is going to be protonated at pH $<$ 8 and de-protonated at pH values greater than the isoelectric point.

Given that the drain current for the SMP surface is lower than the "DYKGGGSH" surface, it can be concluded that the protonation of the SMP linker is higher than that of the peptide for the given pH value. Higher protonation means more positive surface charge, which is mirrored to less majority carrier in the semiconductor channel, thus a lower drain current. However, the complete behavior of the I-V characteristic cannot be fully interpreted, due to the change in APTES transconductance.

4.4 Antibody detection

Since the detection of target biomolecules is desired to take place in physiological salt conditions (1 X PBS), following the surface functionalization with the SMP linker and the "DYKGGGSH" peptide, a first attempt on detecting Antibodies at high salt conditions was conducted. However, given that the Debye length is significantly small (~ 0.7 nm) at this salt concentration and that Antibodies are long molecules, as already described in Section (2.4), the

charge changes occurred outside the ISFETs sensitive area and the Antibodies sensing rendered to be fruitless. As a result, the PBS solution was diluted (0.01 x PBS), increasing the Debye length to $\sim 7.3 \text{ nm}$ and the Antibody detection experiment was conducted again.

As already mentioned in the Section (3.4.4), the tested Antibody concentrations were 0.2 nM , 0.5 nM , 1 nM , 2 nM , 3 nM , 4 nM , 5 nM , 6 nM , 7 nM , 8 nM , 9 nM , 10 nM , 11 nM , 12 nM , 13 nM , 20 nM , 50 nM and 100 nM and the drain current as a function of the different Ab concentrations is given in Figure 4.9.

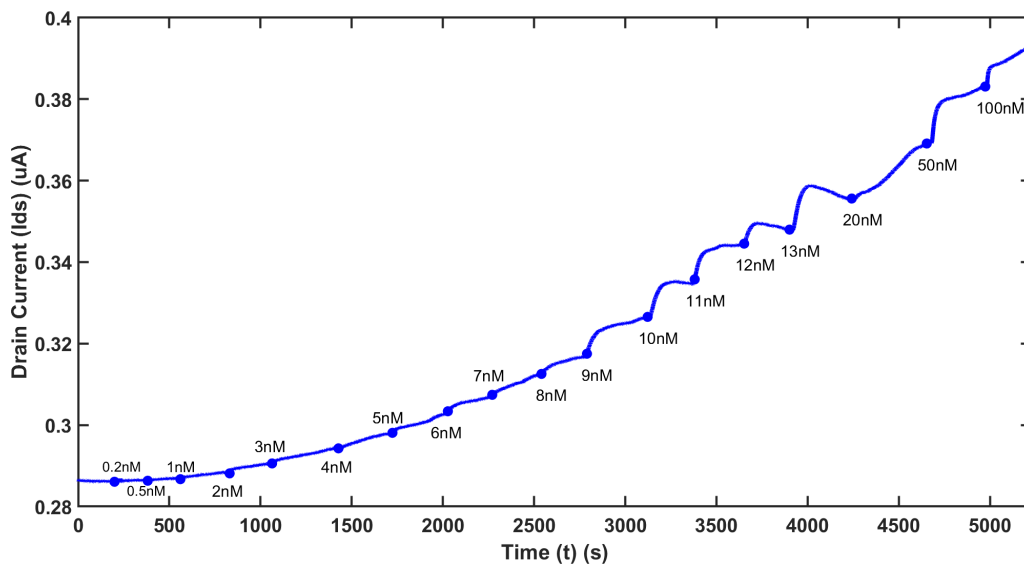


Figure 4.9: The drain current as a function of the Antibody concentration.

For the given chip, the drain current was stabilized after the $\sim 15 \text{ min}$ recording (no drift subtraction needed) and Antibodies were introduced following the current stabilization. It can be clearly seen that, the sensor is sensitive to the Antibody concentration changes with the sensor response starting at $\sim 1 \text{ nM}$, while the drain current is increasing as the Antibody concentration rises.

Furthermore, by plotting the drain current as a function of the Ab concentration, the dose-response curve can be obtained, as shown in Figure 4.10. Specific Ab concentration values have been introduced on the x-axis, so the reader is not confused with the bullet points and the corresponding concentrations. It can be observed that the drain current starts increasing from roughly 1 nM concentration and keeps increasing until approximately 13 nM , where the sensor's surface starts saturating. Even though the surface appears to be saturated at 50 nM , the drain current continues to rise slightly

and this behavior could be due to non-specific binding of Antibodies in other targets molecules, such as the SMP linker, or due to potential dynamic charge interactions between the biomolecules.

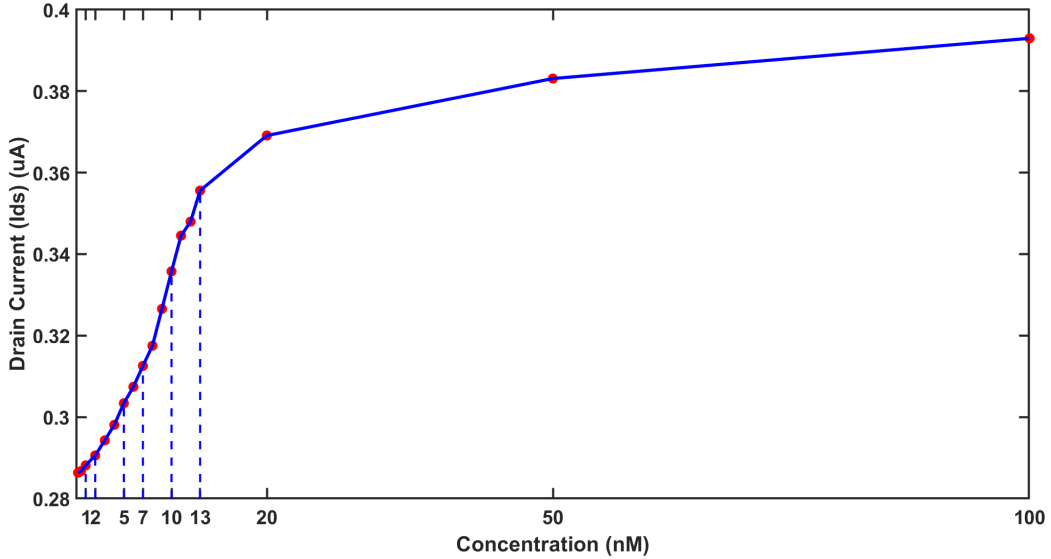


Figure 4.10: The dose-response curve of the sensor.

Based on the experimental work done by Min *et al.*[28], who applied a linear fitting, a similar approach was also implemented on the data. As can be illustrated in Figure 4.11, a linear fitting over the [1-13] nM concentration range, yields a sensitivity of $5.8 \frac{nA}{nM} = 0.39 \frac{\mu A \cdot mL}{\mu g}$.

Finally, the LOD (Limit of Detection) of the sensor can be also calculated by the formula ($LOD = 3.3 \times std/\alpha$), where std is the standard deviation and α is the slope of the fitted curve. Based on this, it can be found that $LOD \sim 0.6 nM = 4.5 \frac{\mu g}{mL}$, while the detection range is $[0.6 - 13]nM = [4.5 - 195] \frac{\mu g}{mL}$, with a sensitivity of $5.8 \frac{nA}{nM} = 0.39 \frac{nA \cdot mL}{\mu g}$, as explained above.

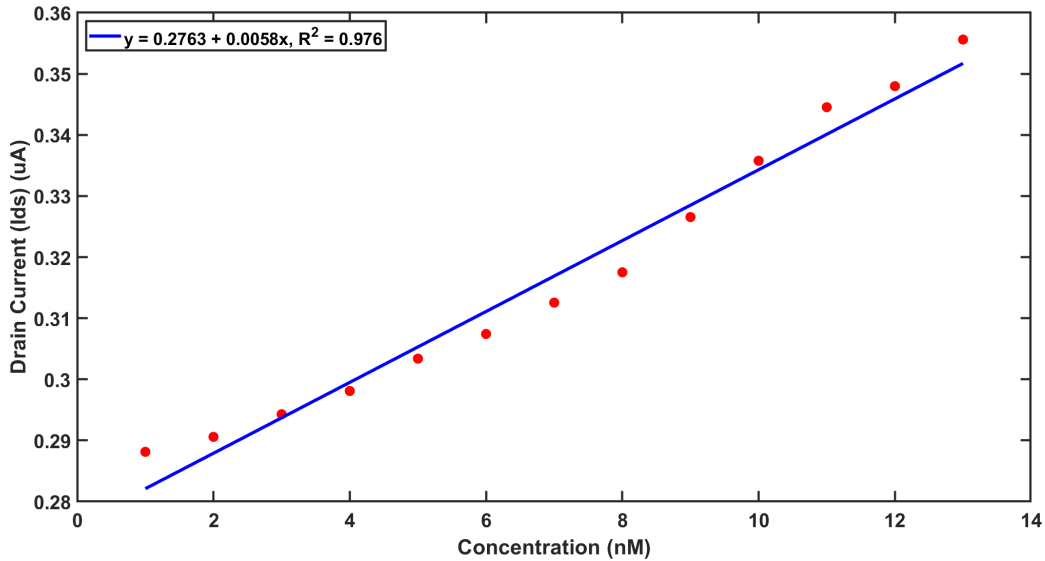


Figure 4.11: The linear fitting of the drain current in the region of [1-13] nM Ab concentration.

4.5 Negative control

In order to validate that the Antibody sensing was successful thanks to the specific binding of the Antibodies to the "DYKGGGSH" peptide and not due to non-specific binding to the surface, a negative control experiment was conducted. Following the SMP linker surface modification, chips were functionalized with PEG-7, as described in Section (3.4.5) and following the drift stabilization, Antibodies were introduced in the following concentrations *0.2 nM, 0.5 nM, 1 nM, 2 nM, 5 nM, 10 nM, 20 nM, 50 nM, 100 nM, 200 nM and 500 nM*. The drain current as a function of the Ab concentration is illustrated in Figure 4.12.

Firstly, the stabilization of the drift can be visualized after ~ 250 min, where the introduction of *0.2 nM* Antibody concentration takes place. It can be observed that, the sensor demonstrates a significantly reduced sensitivity in the [0.2 - 50] nM Antibody concentration range compared to the positive control experiment. However, starting from ~ 50 nM concentration, the drain current increases at a higher rate and from 100 nM the sensor starts exhibiting "jumps" in response to the Antibodies introduction. At these concentrations, the sensor surface is occupied by Antibodies and the non-specific binding of Antibodies to other target molecules, such as the SMP linker takes place, increasing the drain current.

Finally, in Figure 4.13, the dose-response curve of the sensor for the nega-

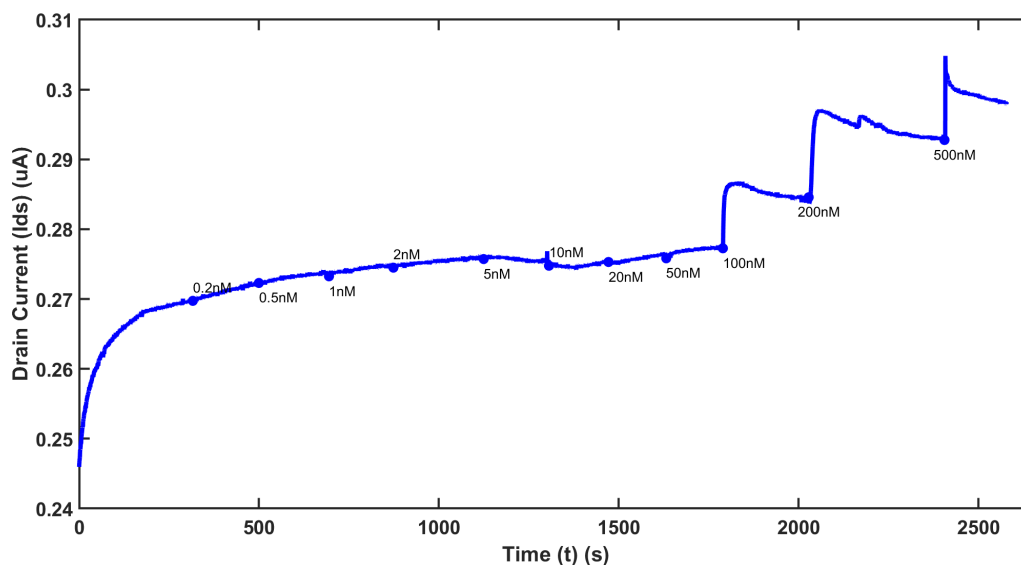


Figure 4.12: The drain current as a function of the Antibody concentration for the negative control.

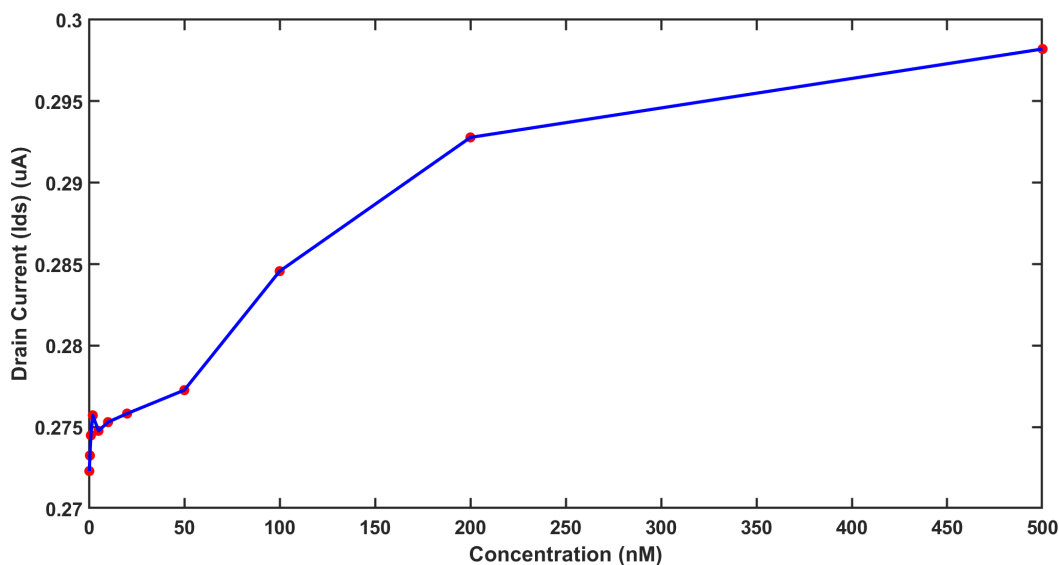


Figure 4.13: The dose-response curve of the sensor for the negative control.

tive control is illustrated. It can be observed that, the sensor is non-sensitive for Antibody concentrations less than 50 nM, while after 100 nM the sensor shows non-specific binding of the biomolecules to the surface molecules. By applying a linear fitting in the [1-20] nM concentration range, it can be derived that the sensor exhibits a sensitivity of $0.75 \frac{nA}{nM} = 0.05 \frac{nA \cdot mL}{\mu g}$, roughly

8 times lower compared to the positive control sensitivity.

Overall, by the negative control experiment it can be concluded that, the Antibody sensing within the [1-13] nM range was successful for the positive control thanks to the specific binding of the biomolecules to the peptide sequence. This can be indicated by the drop in sensitivity for the negative control experiment. Ultimately, at Ab concentrations greater than 50 nM , non-specific binding of Antibodies on the surface takes place, limiting the sensor's sensitivity.

Chapter 5

Conclusion

Within this Master Thesis project, significant advancements towards the implementation of ISFET devices into the "ElectroMed" final prototype were achieved. Bare SiO_2 -gate ISFET devices were characterized in terms of pH sensing and subsequently surface-functionalized for the peptide growth/antibody detection experiments. By comparing the pH sensitivity of the surfaces, it was concluded that the devices could be suitable for the *in situ* peptide synthesis monitoring. In addition, devices were functionalized with a specific peptide sequence followed by the successful sensing of Antibodies in 0.01 X PBS. Finally, via a negative control experiment where the Antibodies sensitivity was reduced, it was demonstrated that the Antibody detection for the positive control was successful thanks to the specific binding of the biomolecules to the grafted peptide sequence. Overall, this Master Thesis project provided a significant insight regarding the ISFET devices abilities as monitoring tools in biochemical processes and as biomolecules detectors and also revealed their limitations under physiological salt conditions. All in all, this project contributed considerably towards the materialization of the "ElectroMed" endeavor.

Chapter 6

Outlook

First of all, since the sensor was able to detect Antibodies successfully, the next step would be the study of the Antibodies affinity to the "DYKGGGSH" peptide sequence. In order to achieve this, an experiment where at $t = t_0$, a known concentration of Antibodies should be introduced and bind to the sensor's receptors, forming Antibody-Peptide ([AP]) complexes (Association, Figure 6.1). Once the signal is stabilized, Antibodies should be flushed away and the sensor should be left to return exponentially to the equilibrium point (Dissociation). The dissociation occurs, based on the fact that protein-protein interactions are not covalent bonds, so the binding is not permanent. For the dissociation "phase", the following equation holds:

$$[AP](t) = -[AP](t)e^{-k_d t} \quad (6.1)$$

where $[AP](t)$ is the concentration of Antibody-Peptide complexes formed at the sensor surface and k_d (1/s) is the dissociation constant. By plotting the time derivative of $[AP](t)$, namely $\frac{d[AP](t)}{dt}$, *w.r.t.* to the concentration of the $[AP](t)$ complexes, the dissociation constant can be derived as the negative slope of the straight line. Ultimately, the dissociation constant is virtually the affinity of the Antibodies to the peptide sequence.

Furthermore, several improvements could be implemented regarding the ISFET devices and the experiment setup. More specifically, devices are highly limited by the drift effect, which reduces the SNR and hinders their prospective biomolecule sensing potential. Based on the fact that SIO_2 experiences the most considerable amount of drift among the oxides because of its porosity, the fabrication of devices with a different gate-oxide could be examined. Moreover, given that Antibodies and buffer solutions were introduced to the open gate-area of the FETs with the use of a pipette during the positive and negative control experiments, final data are susceptible to

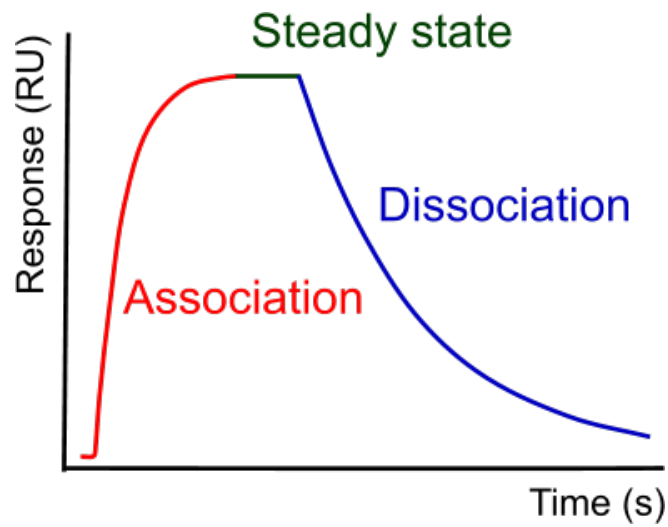


Figure 6.1: The association and dissociation "phase" of an Antibody-Peptide complex[42].

errors and undesired human interference. As a result, a microfluidic setup for the introduction of biomolecules and buffer solutions should be developed, which will limit the undesired effects. Finally, since the final goal of the "ElectroMed" project is the biomolecule detection at physiological salt conditions and not at diluted ones, alternative strategies should be implemented towards that goal, such as the utilization of AC instead of DC voltage input.

Acknowledgment

I would like to express my deepest appreciation to Sergii Pud, Assistant Professor at the University of Twente, for the productive cooperation during the project. His constructive criticism and guidance throughout the project were extremely beneficial in my first steps in reasearch. I am also genuinely grateful to him for showing understanding in my personal circumstances. I sincerely hope in a fruitful collaboration with him in the future.

Furthermore, I am deeply grateful to Rajendra Prasad Shukla, Postdoctoral Researcher at the NC State University, who fabricated the ISFET devices during his postdoctoral research at the University of Twente and helped me in getting acquainted with the lab equipment and the hands-on training during the first two months of the project. The advice and guidance he gave me kept me in the correct path throughout the project. I truly hope to continue cooperation with him in the future.

Moreover, I am really thankful to Dmytro Shavlovskyyi, Researcher at the University of Twente, who developed the LabVIEW software for the pH measurements and characterization of the devices, which allowed the conduction of a plethora of experiments throughout the project. Without his contribution, the project would have been narrower.

In addition, I am also really thankful to Johan G. Bomer, Process Engineer at the University of Twente, for fabricating new devices and for his troubleshooting assistance during the project. I am deeply appreciative to him for being always present when I needed his guidance and advice.

Last but not least, I would like to express my thankfulness to the "ElectroMed" project partners and especially to Janwa El Maiss, R&D Researcher at the Luxembourg Institute of Science and Technology (LIST), who assisted me in the comprehension of the surface chemistry used in the framework of the project.

References

- [1] Sinha, S., & Pal, T. (2022). A comprehensive review of FET-based pH sensors: materials, fabrication technologies, and modeling. *Electrochemical Science Advances*, 2(5), e2100147.
- [2] Schroder, D. K. (2015). *Semiconductor material and device characterization*. John Wiley & Sons.
- [3] Bogue, R. (2013). Recent developments in MEMS sensors: A review of applications, markets and technologies. *Sensor review*, 33(4), 300-304.
- [4] Judy, J. W. (2001). *Microelectromechanical systems (MEMS): fabrication, design and applications*. *Smart materials and Structures*, 10(6), 1115.
- [5] Janata, J. (2010). *Principles of chemical sensors*. Springer Science & Business Media.
- [6] Bedner, K. (2013). *Fabrication and characterization of ion-sensitive field-effect transistors using silicon-on-insulator technology* (Doctoral dissertation, University of Basel).
- [7] Huetting, R. J. E., Vincent, S. E. J., Bomer, J. G., Sanders, R. G. P., & Olthuis, W. (2019). Ion-Sensitive Gated Bipolar Transistor. *IEEE Transactions on Electron Devices*, 66(10), 4354-4360.
- [8] Bergveld, P. (1970). Development of an ion-sensitive solid-state device for neurophysiological measurements. *IEEE Transactions on biomedical engineering*, (1), 70-71.
- [9] Syu, Y. C., Hsu, W. E., & Lin, C. T. (2018). Field-effect transistor biosensing: Devices and clinical applications. *ECS Journal of Solid State Science and Technology*, 7(7), Q3196.
- [10] Rollo, S., Rani, D., Olthuis, W., & Pascual García, C. (2019). The influence of geometry and other fundamental challenges for bio-sensing with field effect transistors. *Biophysical Reviews*, 11, 757-763.

- [11] Hajmirzaheydarali, M., Akbari, M., Shahsafi, A., Soleimani-Amiri, S., Sadeghipari, M., Mohajezadeh, S., ... & Malboobi, M. A. (2016). Ultrahigh sensitivity DNA detection using nanorods incorporated ISFETs. *IEEE Electron Device Letters*, 37(5), 663-666.
- [12] Huang, Y. J., Lin, C. C., Huang, J. C., Hsieh, C. H., Wen, C. H., Chen, T. T., ... & Chen, M. (2015, December). High performance dual-gate ISFET with non-ideal effect reduction schemes in a SOI-CMOS bioelectrical SoC. In *2015 IEEE International Electron Devices Meeting (IEDM)* (pp. 29-2). IEEE.
- [13] Maehashi, K., Katsura, T., Kerman, K., Takamura, Y., Matsumoto, K., & Tamiya, E. (2007). Label-free protein biosensor based on aptamer-modified carbon nanotube field-effect transistors. *Analytical chemistry*, 79(2), 782-787.
- [14] Hideshima, S., Sato, R., Inoue, S., Kuroiwa, S., & Osaka, T. (2012). Detection of tumor marker in blood serum using antibody-modified field effect transistor with optimized BSA blocking. *Sensors and Actuators B: Chemical*, 161(1), 146-150.
- [15] Xu, G., Abbott, J., Qin, L., Yeung, K. Y., Song, Y., Yoon, H., ... & Ham, D. (2014). Electrophoretic and field-effect graphene for all-electrical DNA array technology. *Nature communications*, 5(1), 4866.
- [16] Cheng, S., Hideshima, S., Kuroiwa, S., Nakanishi, T., & Osaka, T. (2015). Label-free detection of tumor markers using field effect transistor (FET)-based biosensors for lung cancer diagnosis. *Sensors and Actuators B: Chemical*, 212, 329-334.
- [17] Shukla, R. P., Bomer, J. G., Wijnperle, D., Kumar, N., Georgiev, V. P., Singh, A. C., ... & Olthuis, W. (2022). Planar junctionless field-effect transistor for detecting biomolecular interactions. *Sensors*, 22(15), 5783.
- [18] Solankia, T., & Parmar, N. (2011, May). A Review paper: A Comprehensive study of Junctionless transistor. In *National conference on recent trends in engineering & technology* (pp. 13-14).
- [19] Hu, C. (2010). *Modern semiconductor devices for integrated circuits* (Vol. 2, pp. 9-24). Upper Saddle River, NJ: Prentice Hall.
- [20] Colinge, J. P. (1990). Conduction mechanisms in thin-film accumulation-mode SOI p-channel MOSFETs. *IEEE Transactions on Electron Devices*, 37(3), 718-723.

- [21] Yannis P.. Tsividis. (1999). Operation and Modeling of the MOS Transistor. Oxford University Press.
- [22] Houk, Y., Iñiguez, B., Flandre, D., & Nazarov, A. (2006). An analytical accumulation mode SOI pMOSFET model for high-temperature analog applications. *Semiconductor Physics Quantum Electronics & Optoelectronics*.
- [23] Baylav, M. (2010). Ion-sensitive field effect transistor (ISFET) for MEMS multisensory chips at RIT. Rochester Institute of Technology.
- [24] Steinegger, A., Wolfbeis, O.S. and Borisov, S.M., 2020. Optical sensing and imaging of pH values: spectroscopies, materials, and applications. *Chemical reviews*, 120(22), pp.12357-12489.
- [25] Van Hal, R. E. G., Eijkel, J. C. T., & Bergveld, P. (1996). A general model to describe the electrostatic potential at electrolyte oxide interfaces. *Advances in colloid and interface science*, 69(1-3), 31-62.
- [26] Van Hal, R. E. G., Eijkel, J. C. T., & Bergveld, P. (1995). A novel description of ISFET sensitivity with the buffer capacity and double-layer capacitance as key parameters. *Sensors and Actuators B: Chemical*, 24(1-3), 201-205.
- [27] Bousse, L., De Rooij, N. F., & Bergveld, P. (1983). Operation of chemically sensitive field-effect sensors as a function of the insulator-electrolyte interface. *IEEE Transactions on electron devices*, 30(10), 1263-1270.
- [28] Min, T. Z. M. M. M., Phanabamrung, S., Chaisriratanakul, W., Pankiew, A., Srisuwan, A., Chauyrod, K., ... & Leelayuwat, C. (2022). Biosensors Based on Ion-Sensitive Field-Effect Transistors for HLA and MICA Antibody Detection in Kidney Transplantation. *Molecules*, 27(19), 6697.
- [29] Hazarika, C., Neroula, S., & Sharma, S. (2019). Long term drift observed in ISFET due to the penetration of H⁺ ions into the oxide layer. In *Pattern Recognition and Machine Intelligence: 8th International Conference, PReMI 2019, Tezpur, India, December 17-20, 2019, Proceedings, Part II* (pp. 543-553). Springer International Publishing.
- [30] Hazarika, C., & Sharma, S. (2014). A mathematical model describing drift in SiO₂ gate pH ISFET's due to hydrogen ion diffusion. *Int. J. Appl. Engineer Res*, 9, 21099.

- [31] Hammond, P. A., Ali, D., & Cumming, D. R. (2005). A system-on-chip digital pH meter for use in a wireless diagnostic capsule. *IEEE Transactions on Biomedical Engineering*, 52(4), 687-694.
- [32] Berg, J. M., Tymoczko, J. L., & Stryer, L. (2012). *Biochemistry* (7th ed., international ed). W.H. Freeman and Company.
- [33] Butterworth, P.J. (2005), *Lehninger: principles of biochemistry* (4th edn) D. L. Nelson and M. C. Cox, W. H. Freeman & Co., New York, 1119 pp (plus 17 pp glossary), ISBN 0-7167-4339-6 (2004). *Cell Biochem. Funct.*, 23: 293-294. <https://doi.org/10.1002/cbf.1216>
- [34] Douglas A. Loy, *Sol-Gel Processing*, Editor(s): Robert A. Meyers, *Encyclopedia of Physical Science and Technology* (Third Edition), Academic Press, 2003, Pages 257-276, ISBN 9780122274107, <https://doi.org/10.1016/B0-12-227410-5/00697-9>.
- [35] Acres, R. G., Ellis, A. V., Alvino, J., Lenahan, C. E., Khodakov, D. A., Metha, G. F., & Andersson, G. G. (2012). Molecular structure of 3-aminopropyltriethoxysilane layers formed on silanol-terminated silicon surfaces. *The Journal of Physical Chemistry C*, 116(10), 6289-6297.
- [36] Sypabekova, M., Hagemann, A., Rho, D., & Kim, S. (2022). 3-Aminopropyltriethoxysilane (APTES) deposition methods on oxide surfaces in solution and vapor phases for biosensing applications. *Biosensors*, 13(1), 36.
- [37] Ashenhurst, J. (2023, February 10). Protecting groups for amines - carbamates. *Master Organic Chemistry*. <https://www.masterorganicchemistry.com/2018/06/07/protecting-groups-for-amines-carbamates/>
- [38] BOC-12-ado-OH =98.0 TLC 18934-81-1. =98.0 TLC 18934-81-1. (n.d.). <https://www.sigmaaldrich.com/NL/en/product/sial/09780>
- [39] Home. A Custom Synthesis Company - Capot Chemical. (n.d.). <https://www.capotchem.com/7087-68-5.html>
- [40] PyBOP CAS 128625-52-5. Luxembourg Bio Technologies. (2023, February 8). <https://www.luxembourg-bio.com/products/pybop/>
- [41] Zeng, S., Wu, F., Li, B., Song, X., Zheng, Y., He, G., ... & Huang, W. (2014). Synthesis, characterization, and evaluation of a novel amphiphilic polymer RGD-PEG-Chol for target drug delivery system. *The Scientific World Journal*, 2014.

[42] Arnoud. (n.d.). A curve. A Curve.
<https://www.sprpages.nl/sensorgrams/a-curve>